Cerebral Blood Flow Measurement Using MRI: Mathematical Regularization and Phantom Evaluation

by

Behzad Ebrahimi

A dissertation submitted in partial fulfillment
of the requirements for the degree of
Doctor of Philosophy
(Biomedical Engineering)
in The University of Michigan
2008

Doctoral Committee:

Professor Timothy E. Chupp, Chair
Professor Douglas C. Noll
Associate Professor Michal R. Zochowski
Research Assistant Professor Scott D. Swanson

To my parents

ACKNOWLEDGEMENTS

I would like to thank all people who have helped and inspired me during my doctoral study. I especially want to thank my advisor, Prof. Timothy E. Chupp, for his guidance during my research and study at the University of Michigan. Even though, I was relatively adventurous at the beginning of my research and I wanted to try every idea I had, he patiently gave me the chance, to explore them and learn how to recognize between practicality and ideality. A special thanks to Dr. Scott Swanson who taught me almost everything I know about MRI. Without his help, many of my experiments would not have been possible. Also, I would like to thank my thesis committee members, prof. Douglas Noll and prof. Michal Zochowski. All my group mates, Eric Tardiff, Monisha Sharma, Robert Cooper as well as my office mate Hau Fo who made our corner (the two offices) a companionable place to work. Many thanks to Bobak Mosadegh and Edward Tang for their enormous assistance with my microfabrication designs. I want to express my gratitude to professors Nikos Chronis and Jeffrey Fessler for their inspiration and help. Folks in glass and machine shops of the physics and the chemistry departments, in particular to Roy wentz, who provided assistance in numerous ways. My deepest gratitude and appreciation goes to my family for their love and support throughout my life; this degree was simply impossible without them.

Behzad Ebrahimi
September 14, 2008
Ann Arbor, Michgan

TABLE OF CONTENTS

LIST OF FIGURES

Figure

LIST OF TABLES

Table

CHAPTER I

INTRODUCTION

Strokes have been the third most prevalent cause of death in developed countries and the second most prevalent cause of mortality worldwide. Verifying the extent and severity of brain damage may be the most challenging problem in the diagnosis and treatment of ischemic stroke victims.

1.1 Ischemic Strokes

Ischemia happens when the brain's supply of oxygen and glucose declines, for any reason, below the normal level. Ischemic tissues usually consist of three compartments. (1) the ischemic core that turns into infarction, (2) the penumbra, an area of moderately ischemic brain tissue which suffers only from functional but not structural injury; and (3) the area of oligemia with preserved neuronal integrity and normal or slightly decreased perfusion that will not turn into infarction [50]. In treating a stroke patient the first step would be to define the penumbra or the area at risk, and then to select the most effective therapy based on the cerebral blood information. The severity of ischemia and the destruction level can be estimated by comparing the quantitative rCBF to threshold values. Electrical failure and membrane failure are two well-known thresholds which mark the upper and lower flow

limits of the ischemic penumbra. Recent studies have suggested a more complex pattern of thresholds to evaluate the degree of destruction [49, 9, 43]. Based on these studies, protein synthesis is inhibited at blood flow rate of 55 ml/100gr/min and is completely suppressed below 35 ml/100gr/min. These values are above the glucose utilization which transiently increases at 35 ml/100gr/min and then sharply declines at 25 ml/100gr/min. This range corresponds to the beginning of acidosis and accumulation of lactate. At 26 ml/100gr/min phosphocreatine and ATP begin to decline. The sodium-potassium ratio of brain tissue increases at flow rates below 10-15 ml/100gr/min. Finally, membrane depolarization occurs when the extra-cellular calcium decreases due to the opening of the calcium channels [4]. Figure 1.1 shows malfunctions due to ischemia that eventually result in cell death.

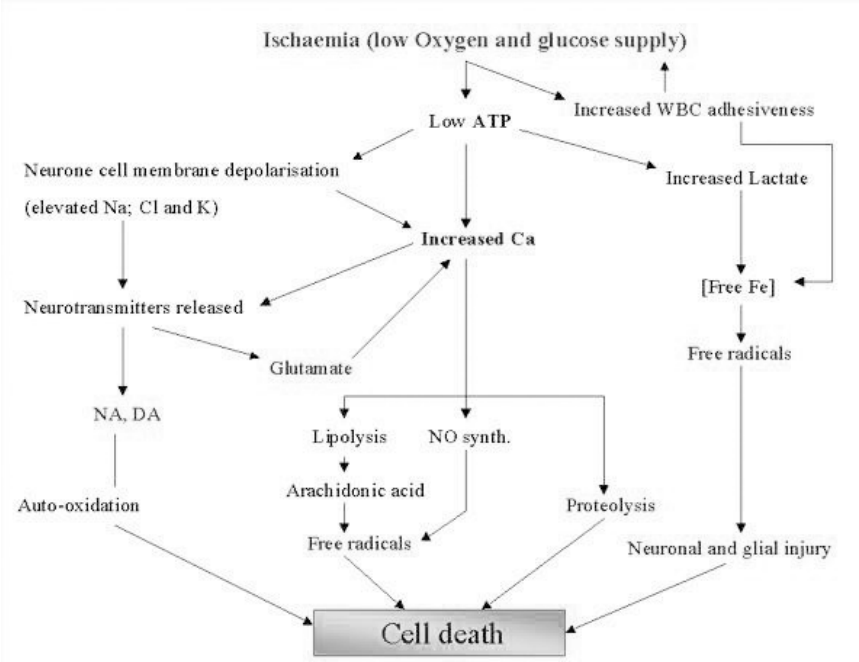

Figure 1.1: Different scenarios which result in cell death due to ischemia. (The Saudi Advisory Group Against Stroke" (SAGAS))

There are many different techniques to determine the extent of a penumbra, table

1.1, [56]. Although none of these techniques are 100% accurate, their results show a rather close correlation. During an ischemic stroke, as CBF begins to decrease, the brain compensates by increasing CBV and MTT to extract more oxygen and glucose. With further reduction in flow, compensatory mechanisms are not sufficient anymore, eventually leading to cellular death. Nabavi and his colleagues showed that the measurement of absolute CBF or MTT, soon after the onset of ischemia, allows the prediction of the size and location of cerebral infarction with good accuracy[44]. Koenig et al. determined that the thresholds for a tissue to turn into infarction or noninfarction are 34 and 62 ml/100gr/min respectively [34]. The ischemic core and penumbra may also be determined based on the measurement of relative values. In this method, the area at risk is estimated based on the mismatch of the diffusion and perfusion weighted images. CBF, CBV, and MTT are parameters which are measured, using Perfusion Computed Tomography, PCT, or perfusion-weighted MRI (PWI) and Apparent Diffusion Coefficient (ADC) is measured, using diffusion-weighted images (DWI). Grandin et al. showed that all these techniques, in regard to their accuracy, are almost equivalent [20].

The quantitative CBF value is also important in selecting the most appropriate treatment [2, 43]. The main idea in ischemia treatment is recanalization, the restoration of the lumen of a blood vessel, and reperfusion of ischemic tissues. The most popular method for reperfusion is IV plasminogen activator (tPA) injection that dissolves the fibrin occlusions. Experiments show that the degree of cerebral blood flow reduction is helpful in predicting the risk of hemorrhage in early reperfusion of severely ischemic regions. Umemura, Suzuka and Yamada showed that regions with residual rCBF lower than 20 ml/100gr/min have damaged connecting tissue which are at high risk of hemorrhage and that the use of thrombolytic would accelerate it seriously[51].

They also showed that regions with residual rCBF at over 25 ml/100gr/min could be recovered by recanalization. Early therapy for patients with reduced rCBF between 25 and 35 ml/100gr/min was recommended; however, for those with reduced rCBF higher than 35 ml/100gr/min, tissue was preserved and no immediate reperfusion was required. For patients with critical hypoperfusion (<10 ml/100gr/min), more aggressive therapies include hypothermia or hemicraniectomy should be considered. Hemicraniectomy is a controversial, radical procedure in which a section of the skull of a stroke patient is temporarily removed to relieve pressure on the brain.

1.2 Perfusion Measurement

Perfusion is a physiological term that refers to the process of nutritive delivery of arterial blood to a capillary bed in biological tissues. In the past six decades, there has been a great deal of interest in cerebral blood flow and perfusion measurement [33, 41, 34, 26, 31]. It has been shown that the measurement of absolute CBF and blood perfusion not only can predict both the extent and the severity of tissue necrosis in ischemic strokes but also may guide physicians to the appropriate selection of treatment [2]. Although it is not yet approved, recent research shows that the reversibility or irreversibility of the damage to tissues in an acute stroke may be determined based on the quantitative measurement of blood perfusion [26, 43]. Due to its noninvasive nature and capability of providing regional information, medical imaging has had a profound impact on CBF measurements.

A number of techniques have been developed to measure perfusion. The main imaging techniques dedicated to cerebral blood flow measurements are positron emission tomography (PET), single photon emission computed tomography (SPECT), xenon-

enhanced computed tomography (XeCT), dynamic perfusion computed tomography, (PCT), dynamic susceptibility contrast MRI (DSC) , arterial spin labeling (ASL) and Doppler ultrasound. These techniques are compared in table 1.1. In 1945, Kety and Schmidt propounded a mathematical model for CBF measurement [33]. The value of tracers in that model depended to a large degree on the rapidity with which they diffuse into tissues. Xenon, due to its biological characteristics including solubility in blood and capability of almost-free diffusion through the blood-brain barrier (BBB), was a great choice. Conn, in 1961, suggested using as a radioactive tracer [23]. Xenon was inhaled or injected, and its clearance signal was recorded at the scalp. The technique made a large impact on cerebral flow measurement at that time. Single photon emission computed tomography (SPECT) with radioactive xenon may be considered as the next generation of that perfusion measurement. The technique has the capability of quantitatively measuring regional CBF. The low energy of the photons (80 Kev) introduces some error to the measurement due to photon attenuation by the brain structure [51]. This problem exists even if more popular and more recent tracers such as 123-iodine and technetium-99m are used. The other disadvantage of this technique is that the spatial resolution of images is low as a result of rapid clearance of the tracers. However, owing to this rapid clearance from the brain, multiple studies can be performed on the same day. The total scanning time is between 10 to 30 minutes. 2D images are usually reconstructed by "filtered back projection" (FBP) process. Images will be corrected for photon scattering distortion and other noise and artifacts using post-processing techniques. The main application of SPECT is the study of acute and chronic cerebrovascular diseases.

PET is another noninvasive diagnostic tool that provides quantitative information on

a variety of hemodynamic parameters such as rCBF, regional cerebral blood volume (rCBV) , regional oxygen extraction flow (rOEF) and glucose metabolism. Tracers are being used for CBF measurements are $^{15}O_2$, $C^{15}O_2$ and $H_2^{15}O$ [37]. The other tracer is ^{18}F in fluorodeoxyglucose which is used to monitor glucose consumption in cancer evaluation [56]. Data acquisition takes typically 5 to 10 minutes and it takes another 5 to 10 minutes to obtain a processed CBF map. The main advantage of PET is the accuracy and reproducibility of its results even in voxels containing major vessels or regions of brain with altered perfusion or metabolism. Computed tomography (CT) using stable ("cold") xenon started in the 1970s. Xenon attenuates x-ray in a manner similar to iodine. Therefore it is used as a contrast agent and at the same time as an inhaled tracer for perfusion measurements. To prevent the anesthetic effect of xenon, a mixture of 28% xenon and 72% oxygen is most commonly used. XeCT produces images with much higher spatial resolution than SPECT. Superposition of the numerical data and the anatomical image yield a map of quantitative flow tightly coupled to cerebral anatomy. The capability of measuring absolute CBF is another advantage of this technique. CT has the ability to provide measurements of equal validity within the cortex as well as the depth of the brain. Yet, it doesn't have the ability to evaluate cell viability and functionality unlike PET and MR based methods. Since the blood flow in a single voxel is very unstable, reproducibility is evaluated by comparing the average measured perfusion over at least 100 voxels. In xenon enhanced CT the reproducibility of the data from a region larger than 1 mL is about 12%. This value in PET and SPECT is 5-10% and in MR-related techniques is 10-15% [56]. Perfusion computed tomography (PCT) is another CT-related technique used for brain hemodynamic measurements and imaging. It uses first-pass tracer methodology and is based on the Meier-Zierler mathematical

model [41]. In an imaging session a bolus of 40 to 50cc of 300-370 mg/dL of iodinated contrast agent is injected intravenously. The total scanning takes 40-45 seconds with a scan rate of one image per second. One of the advantages of PCT over XeCT is that besides CBF it can be used to measure CBV, mean transient time (MTT) and time to peak (TTP) as well [34].

Today, magnetic resonance imaging is also used for perfusion measurements. There are two major measurement techniques: dynamic susceptibility contrast (DSC) (also called bolus tracking) and arterial spin labeling (ASL). These MR based techniques use Meier-Zierler and Kety-Schmidt models for regional CBF calculations. In DSC imaging a paramagnetic material produces dephasing in a small area around the tracer in its first pass and as it moves in vessels it affects the T_2^* in adjoining tissues. Perfusion can be measured based on the change in the MR signal. Just like XeCT, DSC can be used for relative CBV, TTP and MTT measurements as well. To measure absolute quantitative values, the arterial input function (AIF) is required. AIF is the concentration-time curve of the tracer in the artery supplying the tissue. The technique requires fast imaging sequences such as echo planar imaging (EPI). Images are taken in the rate of 500 ms to 2 seconds per single image. In ASL water proton spins in the extra-cranial blood are inverted by applying RF pulses. The change in magnetization can be calculated by subtracting the images taken before and after the labeled blood mixes with the extra-vascular blood in the cranial plane. This magnetization change is proportional to the blood flow. A newer approach has been proposed for blood magnetization inversion based on blood velocity. One shortcoming with ASL is its lack of accuracy in mapping blood flows lower than 10 mL/100 g/minute due to the slow water exchange. The difference between labeled and control acquisitions is about 1% of the control signal intensity. The method

suffers from low signal to noise ratio.

The last technique, Doppler ultrasound, is a noninvasive method which is used for global CBF investigations. The technique is operator dependent. However, the blood flow volume (BFV) showed a close linear correlation with hemispheric CBF measured using xenon. The greatest advantage of that is that it can be easily performed at a patient's bedside.

Our group has pursued a new MR-related technique to measure absolute rCBF, with application in ischemic strokes diagnosis and treatments, using polarized xenon as a magnetic tracer. Most of the techniques mentioned above use exogenous tracers (tracers developed from outside the body) as contrast agents. Xenon in XeMR is more than just a contrast medium. Much spectroscopic information can be extracted from its NMR signal. For example, owing to its large and environment sensitive chemical shift, CBF for different tissues can be measured distinctly. Also, CBF maps in the other MR-related techniques suffer from low signal to noise ratio because of the small differences between the labeled images and the control (background) ones. As mentioned before, in this approach, the polarization of xenon is enhanced up to five orders of magnitude compared to its thermal polarization. Since there is no source of xenon in the body, no background signal is expected, promising higher SNR in the images. In regards to the data acquisition, the technique will have the flexibility to trade off spatial against temporal resolutions based on clinical priorities. For maximum benefit to interpretation, low resolution CBF maps need to be superimposed over high resolution anatomical images. In contrast to PET and SPECT, which need other equipment for taking high resolution anatomical images, in XeMR the same MRI machine may be used for the both purposes. for cavities MRI using xenon polarized noble gases is the only option. At this moment, polarized xenon and helium

are among very few possibilites for perfusion imaging in lung studies.

Just like any other technique, XeMR has its own disadvantages. If the in vivo T_2^* is short, it limits our ability to use ultra-fast imaging pulse sequences [40]. The other problem with using xenon is that it is not yet approved by the FDA. For the time being it is only available under the investigational new drug (IND) status. Xenon's short T_1 relaxation time in vivo is another problem with this technique. The T_1 in blood is about 5 seconds. Xenon transfer from the lungs or veins to the brain alone takes several tens of seconds, which destroys a considerable amount of polarization. To minimize this problem, several nontoxic carriers of xenon including intralipids, liposomes, and Perfluorooctylbromide (PFOB) have been suggested [58]. Among these carriers, xenon has the longest in PFOB emulsion. If the droplets of PFOB are in the range of 5-10 microns the NMR signal will be the among the carrier solutions.

1.3 Blood Flow Estimation and the Mathematical Limitations

CT and DSC MRI use Meier-Zierler perfusion model for flow estimation. This model links the tracer dilution to the blood flow rate. The model can be expressed in the form of an integral equation which is the convolution of the two functions; residue and arterial input function multiplied by the flow rate. We will discuss these two functions and their characteristics in detail in the third chapter.

Since the time Paul Meier and Kenneth L. Zierler proposed their model, back in 1954, many attempts have been maded to find the deconvolution algorithm that overcomes the limitations of this problem, which have roots in the instinctive instability of Fredholm first kind integrals, in the presence of noise. These types of problem is referred to as an ill-posed problem, and will be carefully studied in chapter III. Integral

transforms were among the very first approaches which were tried by researchers for deconvolution. the Laplace transform was used by Grodins, Fleming and Goddard [19, 17]. The Fourier transform was investigated by Anderson et al. [3] These model-free methods faced problems that many of them are not yet resolved. Using discrete least square methods for this purpose was initiated by Diffey et al. [12] in 1976 that used the matrix algorithm described by Valentinuzzi and Montaldo Volachec [52] to linearize the problem. Need for such methods were felt even more when it turned out that transform-based methods underestimate flow rate and are not as capable in smoothing. Bronikowski et al. used conventional mathematical deconvolution and stabilized it using damped least square method. Also, they were among the first groups who studied the delay effect[8]. The time interval between the tracer concentration measurement in the artery supplying the tissue and the observation of the tracer in the tissue is referred to as "bolus delay" in MRI literature. This problem usually results in flow underestimation and will be discussed in detail in chapters III and IV. Kuruc et al. in 1983 implemented a model based approach in combination with a least square based smoothing method [1]. They suggested the "lagged algorithm" which can be referred to as a first generation of our method. Although Singular Value Decomposition (SVD) was well-known by many mathematicians long before (in the original form by Kogbetliantz in 1954, 1955 [35] and Hestenes in 1958 [25] and in the more practical form by Golub and Kahan (1965) [18] and many groups had already revealed their interest in least square based techniques by this time). It wasn't until 1987 and by Van Huffel et al. that SVD was introduced to the field of perfusion measurements[27]. Even for few years after that, many of the researchers such as Bock et al.[6], Juni et al.[30], Puchal et al. (1988) [48] and Bates in 1991 [5] preferred other methods for deconvolution. SVD is a powerful matrix factorization

method which is computationally inexpensive. This method was introduced to MRI community by Ostergaard et al. in 1996[46]. The brilliant idea, which Ostergaard and his colleges, and previously, Diffey and Van Huffel, had adopted from Valentinuzzi and Volachec's work[52], was writing the perfusion convolutional equation in the form of a linear matrix equation, since SVD can only be applied to linear problems. Their simulations and experimental results showed that SVD, similar to other least square methods, is sensitive to the bolus delay. Later, to improve the delay sensitivity, the Block-circulant SVD was introduced by the same group [59]. Today, Truncated SVD is the most popular method for perfusion model deconvolution. In this method, to stabilize the solution, terms corresponding to frequencies higher than a threshold frequency are discarded. The method is simple and computationally inexpensive. However, some major shortcomings in this method have convinced researchers that investigation for more robust methods should be continued.

In 2003, Calamante et al. used Tikhonov regularization for the flow estimation and residue function deconvolution[10]. Tikhonov regularization which can be categorized under the "small derivatives" regularization methods has a great capability in removing the oscillations from residue functions. It also preserves the shape of the residue function, which is important in vasculature heterogeneity study in tumor treatment, better than any other regularization. Although Tikhonov regularization showed very promising, it suffers from an assumption which is not always valid. As mentioned before, in this method it is assumed that the derivatives of the residue functions are small. This is not true when the mean transition time is short or the temporal resolution is low. The misassumption results in a flattening of the residue function, which consequently gives rise to flow underestimation. Maximum likelihood estimation (MLE) is another method which has recently been used by researchers.

MLE is a statistical method which chooses the residue function that has the highest probability. What this method calculates is actually the distribution of the elements. To keep the elements deviation tight, some a priori information including the type of the distribution of the elements is required. Gaussian process deconvolution (GPD) [3] and Bayesian estimation [42] are two instances of this approach.

Using the Tikhonov framework, we have suggested a method to correct the small derivative misassumption in regular Tikhonov regularization [13]. This approach opens a window to introduce more priori information to the method. Such a priori information compensate for the information distorted by noise. We believe, although model independent methods considerably improve the stability of the solutions, the information lost due to the presence of noise cannot be retrieved unless a priori information is used. A comprehensive model that includes the effect of delay and dispersion is applied which can improve the quality of the residue function as well as the flow estimation. This method is not as computationally efficient as TSVD is but slightly longer computation time is the least price which could be paid for a more sophisticated method. Since perfusion measurement using imaging can be processed in a very parallel manner we are hoping new multiprocessor computers improve the calculation time issue as well.

Table 1.1: Comparing the strength and weakness of different perfusion imaging modalities [56]

	Strength	**Weakness**
PET	Accurate Quantitative measurements. Assessment of multiple factors using various radioligands. Repeated measurements possibly attributable to short half-life of radiotracers.	Impossible to use in the emergency settings. High cost (however, cost-effective in well-established diagnostic algorithms).
SPECT	Technetium generator widely available. Can be used at bedside and in the emergency. Setting Low cost.	Relative, not quantitative measurements. Poor spatial resolution.
XeCT	Accurate quantitative measurements. Assessment of multiple brain levels. Can be repeatedat 10-minute intervals providing an ability to measure the CBF response to interventions.	Relatively long acquisition time, prone to motion artifacts. Inhalation of Xenon via a face mask. Xenon not currently approved by the FDA (technology only available at this time under IND status)
PCT	Wide availability of necessary equipment, including in the emergency setting. Access to multiple perfusion parameters (CBV,CBF, MTT). Accurate quantitative measurements.	Presently limited anatomic coverage. Use of ionizing radiation and iodinated contrast media.
DSC	Can be combined with fine anatomic imaging, DWI, MRA, spectroscopy, providing the most comprehensive information in one examination. Repeatability (attributable to a lack of ionizing radiation). Whole brain coverage.	Lack of standardization in the interpretation. Not available in the emergency settings in most institutions. Difficulties associated with obtaining MRI (claustrophobia, contraindications, and access issues).

Table 1.1 Continue..

	Strength	**Weaknesses**
ASL	Repeatability (attributable to a lack of ionizing radiation). Noninvasiveness (no intravenous injections). Flexibility (spatial resolution and imaging time can be traded off depending on the clinical question).	CBF underestimation associated with extremely delayed arterial arrival times (such as through collateral pathways). Relatively low signal-to-noise ratio per unit time. Difficulties associated with obtaining MRI (claustrophobia,contraindications, and access issues)
XeMRI	Flexibility (spatial resolution and imaging time can be traded off depending on the clinical question). Repeatability (attributable to the lack of ionizing radiation). Can be combined with fine anatomic imaging, spectroscopy, providing the most comprehensive information in one examination	Xenon is not currently approved by the FDA. The technology is only available at this time under the IND (investigational new drug) status. Xenon polarization takes time and equipments. Difficulties associated with obtaining MRI (claustrophobia, contraindications, and access issues).
Doppler	Can be performed at bedside. Repeatability (attributable to a lack of ionizing radiation). Noninvasiveness (no intravenous injections).	Provides only one value for each brain hemisphere. Operator dependent.

CHAPTER II

POLARIZED XENON

Xenon is an inert gas that has the capability of polarization enhancement up to five orders of magnitude. In addition, xenon is nontoxic and it is being characterized by a high solubility in lipid, large chemical shift and high sensitivity of its chemical shift to its environment. All these advantages of working with xenon together with its high capability of polarization make it a valuable tool for medical researches.

2.1 Experimental Setup

Optical pumping - In this process an alkali-metal (here Rb) valance electrons are polarized by circularly polarized laser beam. As shown in figure2.1, laser photons excite transition D1 (795 nm inRb) which sends the ground state electrons $m_j = -\frac{1}{2}$ to the $m_j = \frac{1}{2}$ excited state . The excited state decays or collisionally de-excites to the ground state. This polarization will be transferred to the noble gas nuclei through hyperfine interaction between gas nucleus and valance electrons of alkali-meta. Quenching with nitrogen buffer gas repopulates both ground-state sublevels through non-radiative de-excitation collisions with almost equal probability.

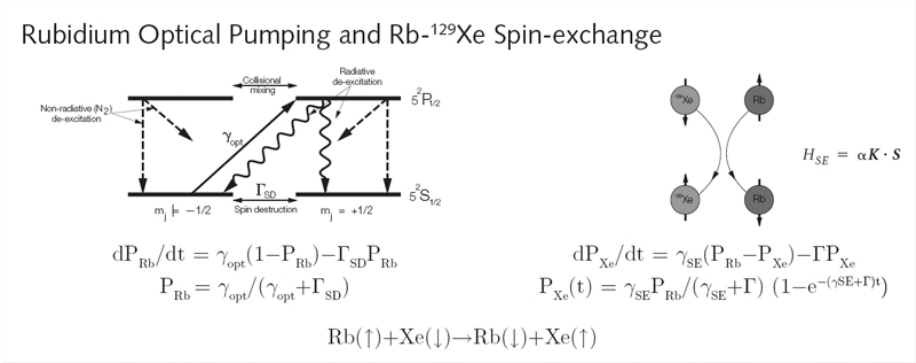

Figure 2.1: Xenon optical pumping. The energy of the laser photons is deposited in rubidium electrons and then it is transferred to xenon through a hyperfine interaction.

2.1.1 Optical Pumping Cell

A Schematic drawing of our optical pumping system is shown in Figure 2.2. The optical pumping cell (OPC) is a 17cm long, 25 mm inner diameter Pyrex cylinder 0f $\sim$75 cc volume with flat end windows. A Pyrex sidearm for Rb loading is attached to the center of the cell, transverse to the plane of the valves. A Pyrex outer jacket serves as an oven. Two glass high vacuum valves (Chemglass, Inc., Vineland, NJ) are mounted transverse to the long axis near each end of the cell. These valves permit the cell to be evacuated and filled at one end and polarized Xe to be delivered at the other end. The cell is chemically cleaned and internally coated with octadecyltrichlorosilane (OTS) to minimize depolarizing ^{129}Xe-wall interactions. A Pair of Helmholtz coils provides the uniform magnetic field needed for optical pumping. The current for the coils is supplied by a 400 watt power supply. The magnetic field at the center of the OPC is about 18 gauss and slightly different at the ends. The relaxation rate at the walls, Γ_{wall}, is strongly dependent on the magnetic field. The spin exchange rate,γ_{SE}, varies from 5×10^{-4} Hz at 80℃to 7×10^{-3} Hz at 120℃. For optical pumping $\Gamma_{wall} \ll \gamma_{SE}$ is required. We will show later that although the spin-exchange rate increases with temperature, there is an optimum temperature

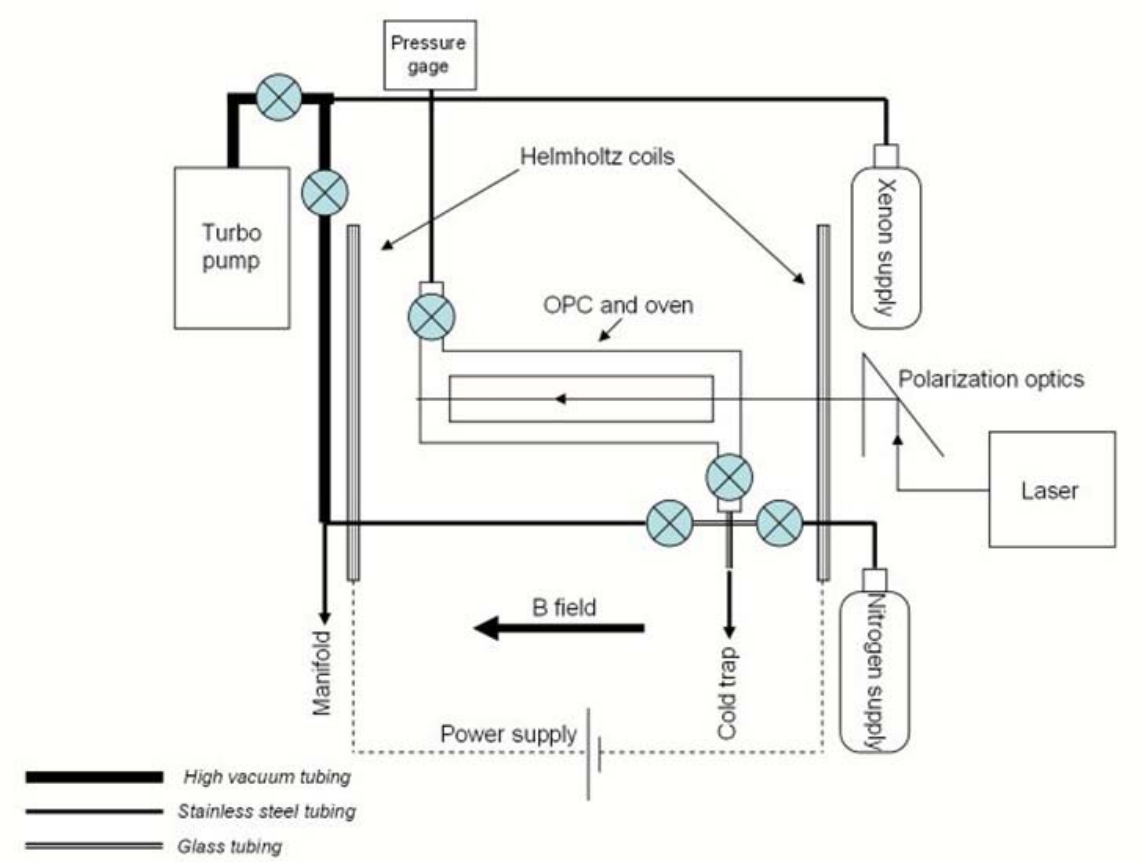

Figure 2.2: Polarizer setup. OPC is the heart of the system. Central part of the cell is surrounded with a heat jacket that provides a uniform temperature to the cell. Two Helmholtz coils provide a uniform magnetic field which is required for optical pumping.

that results in the maximum polarization. It decreases for higher temperatures due to the dominancy of spin-exchange destruction of rubidium vapor. A PID temperature controller is used to hold the temperature at its optimum point. Attached to a sensor, placed in the oven jacket, this reads the temperature in real-time. The power needed to stabilize the temperature is calculated by the PID program and supplied by the heater. The heating system is a 750 watt standard hot air heater (Hotwatt Inc., Danvers, MA). Air passes through electrically heated elements and then the hot air is transferred to the jacket through a silicon hose. The optical pumping starts by irradiating the OPC using a LDA (Opto Power, Tuscon, AZ). It provides 15W of cw laser light with a 2-3 nm full width at half maximum (FWHM). The LDA light

is circularly polarized and incident on the OPC flat window.

2.1.2 Delivery Line

The delivery line includes 4 major components; a cryogenic cold trap, a pressure stabilizer, a mixer (dissolver) and tubing.

Cryogenic cold trap - Polarized xenon needs to be separated from the other buffer gases in the OPC. These buffer gases are usually nitrogen and helium. The freezing point for both of these gases is lower than that of xenon. One approach to separating these gases is to freeze xenon with liquid nitrogen and pumping the other gases out of the container. However, for the best results several things need to be considered when designing a cold trap. The gas-liquid nitrogen contact surface should be as large as possible compared to the container volume. There are two reasons for such a design. First, it decreases the diffusion distance for xenon atoms to reach the walls, where they are supposed to freeze. The freezing process can also be accelerated by choosing a coarse contact surface instead of a smooth one to take the advantage of turbulence. Second, as the frozen xenon layer on the walls gets thicker the temperature at the distal side decreases. The xenon relaxation time decreases dramatically around its melting point [38]. Figure 2.3 shows that after 15 min of accumulation at 0.06 T, the magnetization is about 50% of the no-loss limit. Figure 2.4 shows the design of cryogenic system. It has two major components; the cold trap and the heating system. The cold trap consists of two coaxial tube inlet (inner tube) and an outlet (outer tube). Both tubes are placed in thermally insolated jackets to prevent freezing of xenon anywhere except the container which is placed at the bottom of tubes. This container is submerged in liquid nitrogen. After the cold trap is pumped to 10^{-7} Torr or less, the polarized xenon is led through Teflon tubing to the cold trap. After a few seconds the remaining gas mixture in the tubing is chased by puri-

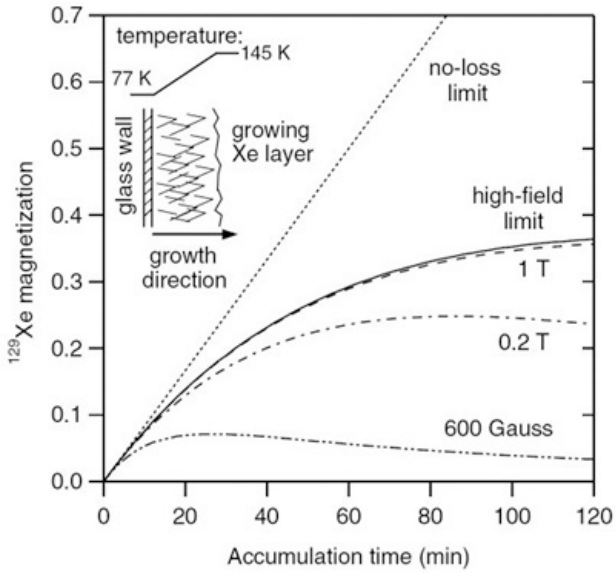

Figure 2.3: Xenon polarization/relaxation over time. The polarization/relaxation of the xenon stored in liquid nitrogen temperature is a function of the magnetic field applied to the storage. Also, along the growth direction the temperature drops quickly from liquid nitrogen temperature to the xenon melting temperature which results in faster relaxation towards the center of the cold trap [38]

fied nitrogen gas to the cold trap. Then the nitrogen is pumped out from the other side. This process is repeated several times until enough polarized xenon accumulates. As mentioned above the xenon relaxation time at the transition temperature is very short. It's even shorter than the gaseous T_1 in the same magnetic field. As a result, the transition from solid to gas should take place in the shortest possible time to minimize the polarization loss. The heating system consists of two hot air exhausts and a spiral tube. The exhausts warm up the part of the container which is out of the liquid nitrogen to accelerate the evaporation. The spiral part controls the liquid nitrogen evaporation. The temperature right above the liquid nitrogen can reach around 30℃. In such a huge temperature gradient, the transition happens in a fraction of second.

Magnetic field design - The relaxation time is strongly dependent on magnetic field.

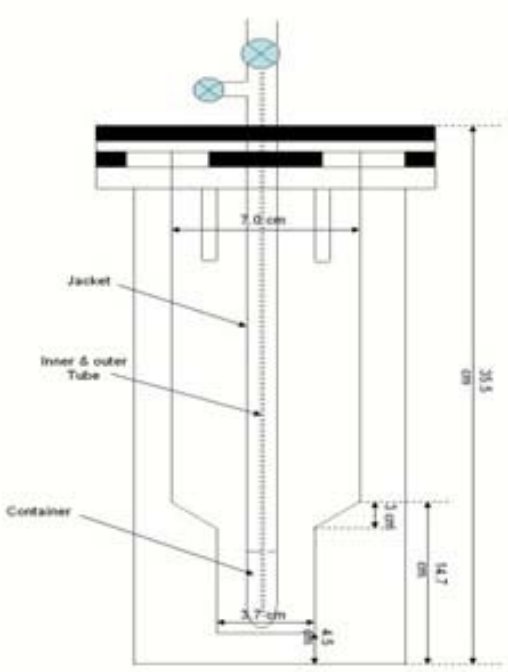

Figure 2.4: The cryogenic system. Two coaxial tube in the central part provide a path for the gas mixture to the nitrogen bath. Xenon freezes on the wall at the cold trap at the lower part and the buffer gases are vacuumed out of the cold trap.

In laser polarized xenon accumulation, long T_1's are desired. The homogeneity issue is more important in gaseous xenon storage, while in solid xenon accumulation field strength is the dominant factor. Depending on the amount of LP xenon needed for experiments and the accumulation times, xenon might be kept frozen for one or more hours in the cold trap. We have tried three different ways to provide a strong magnetic field over the storage area. Helmholtz coil combinations, which consist of 4 pairs of coils to overcome the current limit in single pairs, provide a very uniform field. Using Biot-savart, the magnetic fields were simulated. Simulation results showed B_x and B_y components would be almost zero even for hand-wound coils. A second, and a more practical method, was to use the MRI field fringes; but they do not produce a uniform field as coils do. The third option was to design the field using permanent magnets. Pressure stabilizer - After thawing, xenon is stored in a 75cc Pyrex cylinder. The cylinder splits into two compartments by a piston. In one

compartment xenon is stored and the other one is pressurized by nitrogen. Since the gases on both sides of the piston are in equilibrium, the xenon pressure can be controlled. Also any fluctuation in pressure is measured from the nitrogen side by a ASDX015A24R sensor (Honeywell system) for later corrections to the results.

Mixer - To inject xenon as a magnetic tracer it needs to be dissolved in a biologically friendly solvent. We use PFOB as our solvent because it is biologically harmless, it has high xenon solubility and the xenon relaxation time in PFOB, although still much shorter than relaxation time of gaseous xenon, is longer than in other currently available options. For steady-state applications, xenon needs to be dissolved right before the injection, which is why we have designed and built the mixer. PFOB is injected and pressurized in the mixer using a syringe driver. Xenon pressurized in the storage cylinder is led through a piece of Teflon tube to the mixer and then pressurized even more by a capillary that takes polarized xenon into the solvent. Xenon bubbles in the solvent and dissolves few seconds before delivery to the target in the MRI system.

Tubing - Most of the components of the delivery line are connected to each other by Teflon tubing. The xenon T_1 in Teflon tubes is almost 125 seconds. It is much shorter than the T_1 in glass even without coating. Since the flow in some parts of the delivery system is very slow and using Teflon tubing as a flexible and quick way of connecting components has been inevitable, we have used very thin tubes, 0.03" O.D, to minimize the flow time in the tubes. In the final setup some of them will be replaced with OTC coated glass tubes.

2.1.3 Xenon Carrier

The line width of xenon dissolved in PFOB NMR signal is dependent of the droplets' size. The goal was to make PFOB droplets 5-10 micron in diameter as xenon carriers since they produce the sharpest peaks. We mixed 20% perflurooctylbromide 99% (Sigma-Aldrich Inc.) with 2% Pluronic solution 10% (Sigma-Aldrich Inc) and 78% Saline. Then we placed the solution in a shaker for 45 seconds. Right after the shake solution was in foam phase but after 10-20 minutes three phases appeared. Remained foam at the top, liquid phase in the middle and droplets settled at the bottom. Figure 2.5a shows the droplets made using this method.

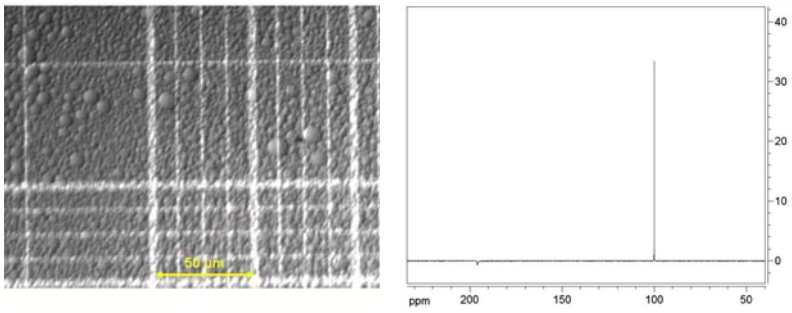

(a) (b)

Figure 2.5: (a) PFOB microbubbles. Mixed 20% perflurooctylbromide 99%, 2% Pluronic solution 10%, and 78% Saline. And shaking for45s microbubbles with diameters $\leq$ 10m were generated. (b) The NMR signal of LP xenon dissolved in PFOB. The peak at 100 ppm belongs to xenon in PFOB and the other peak at 200 ppm comes from xenon in saline.

As mentioned before, PFOB is non-toxic. It has high xenon solubility and longer than other carriers currently available. To study the LP xenon in PFOB, droplets in the abovementioned solution were separated from the liquid and the foam. After partially degassing them, LP xenon at 2 atm pressure was added. Figure 2.5b shows the spectrum of laser polarized xenon in PFOB taken by our NMR Bruker system. The peak at 100 ppm belongs to xenon in PFOB. There is also another peak at 200 ppm which comes from xenon in saline.

2.2 Simulations

In the following two sets of simulations will be studied. The first set represents the polarization level as a function of the laser power, buffer gas pressure and the cell temperature. The goal is to find the optimum value for these parameters to optimize the rubidium and xenon polarization in the process of optical pumping. Figure 2.6. shows, different phenomena involved in this problem. The second set, simulates the

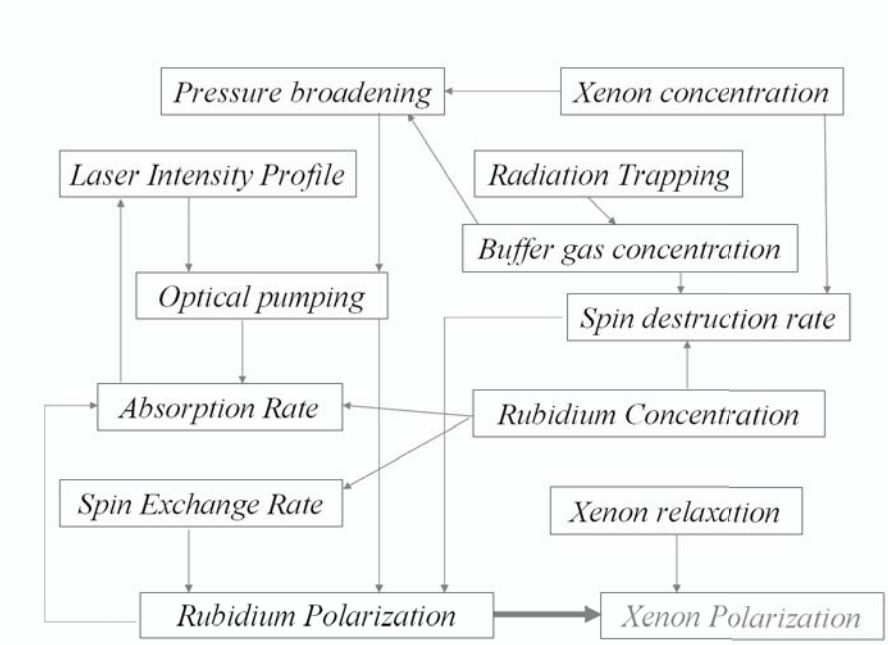

Figure 2.6: The chain of parameters in optical pumping. Depending on the goal very different approaches might be chosen.

steady-state polarized xenon imaging, using a continuous source of polarized xenon and. Perfusion-related parameters measurement is simulated. We will show that RF pulse effect correction is required to calculate correct blood volume and mean transition time. We will also show since these two will be affected equally the ratio of them which gives the blood flow rate will remain unaffected [14].

Simulation I - The level of polarization achieved via optical pumping mainly depends on the laser power, buffer gas pressure and the cell temperature. The scattering rate

of rubidium atoms is a function of the laser profile:

$$\gamma_{opt} = \int \Phi_z(\nu, z)\sigma d\nu \tag{2.1}$$

where Φ_z is the scattering cross section and Φ is the laser profile. The scattering cross section is a function of buffer gas pressure. Raising the helium and nitrogen pressure broadens the rubidium D1 line and increases the laser-atom interaction cross section. In the other words, it increases the scattering cross section and the laser profile overlapped area in the frequency domain. This overlapped area is proportional to γ_{opt}. The rubidium polarization is

$$P_{Rb} = \frac{\gamma_{opt}}{\gamma_{opt} + \Gamma_{SD}} \tag{2.2}$$

where is the spin destruction. Spin destruction is also a function of buffer gases molar concentration [54].

$$\Gamma_{SD} = k_{Rb-He}[He] + k_{Rb-N_2}[N_2] + k_{Rb-Xe}[Xe] \tag{2.3}$$

which k's are the rate constants for spin destruction due to collisions with each species and bracket terms are molar concentrations of each species. As the equation 2.1 shows, to obtain high polarizations in an optical pumping process, the scattering rate needs to be very large comparing to the spin destruction rate. Rubidium-rubidium interaction is the major contribution to spin destruction. To keep this term small, the rubidium concentration (or its partial pressure) should be kept small. It can be controlled via the oven temperature, since the vapor pressure is a function of temperature. It is a tradeoff problem. Rubidium-xenon spin destruction gives rise to Γ_{SD} for high xenon concentration. So for large amounts of xenon, polarization will be limited. If the amount of xenon needed for the experiment is known, the other parameters can be calculated or simulated to optimize the polarization. Figure 2.7

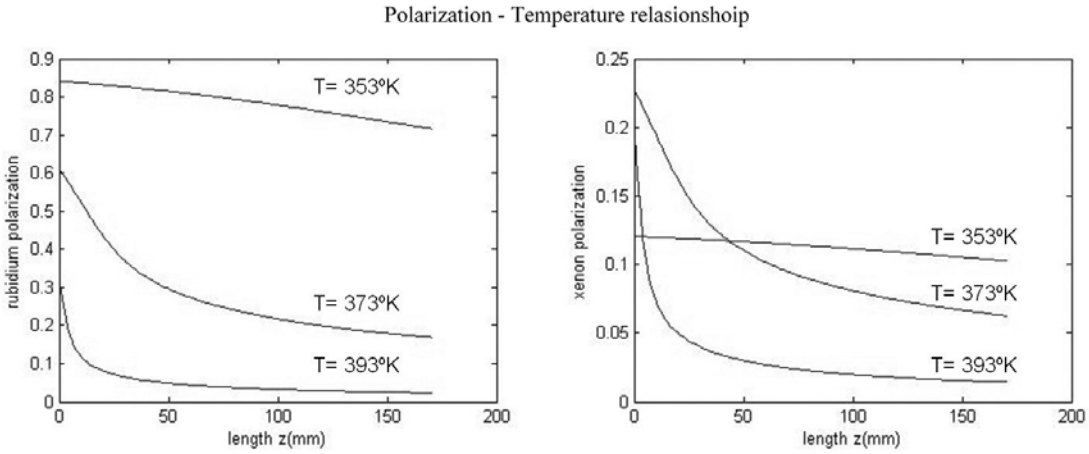

Figure 2.7: (Left) Rubidium (Right) xenon polarization at different temperatures.

shows the simulation results of polarization along OPC "z" axis. As figure shows the polarization drops along the axis because of the absorption of the laser photons by rubidium atoms. This attenuation is much faster at higher temperatures because of the higher rubidium vapor pressure.Even with high laser power polarization happens mainly close to the front window at such temperatures. Although rubidium polarization is higher at lower temperatures, the optimum xenon polarization is usually found in higher temperatures. This is because the spin exchange rate is proportional to the rubidium concentration, and its vapor pressure. With a sensor at the back window the laser profile can be recorded. The D1 linewidth can be calculated by comparing the profile at the front and back windows. For LDA's the line width is about 2 nm which is much broader than D1 line. As mentioned before, the D1 line can be broadened by high buffer gas pressure; however, for feasible gas pressures D1's linewidth will still be much smaller than the laser bandwidth. Polarization is also a function of laser intensity. Figure 2.8 shows this dependency for three different intensities. As mentioned before, rubidium scattering is a function of laser intensity and its spectrum. Very high laser beam intensity, even with a wide bandwidth, can

provide enough photons to keep all the rubidium atoms continuously excited. In other words, the spin scattering rate will be much greater than the spin destruction rate. Simulation II - This model was developed by our group to describe the magnetization in the brain. We will use this model to study the effect of the RF pulses on the estimation of perfusion-related parameters. In the following we will briefly discuss the perfusion model and then, using a simulation, we will show the effect of RF pulses on the measurement of perfusion-related parameters. A detailed discussion on perfusion models and the mathematical technique, singular value decomposition, used in calculation can be found in chapter III. The model is based on

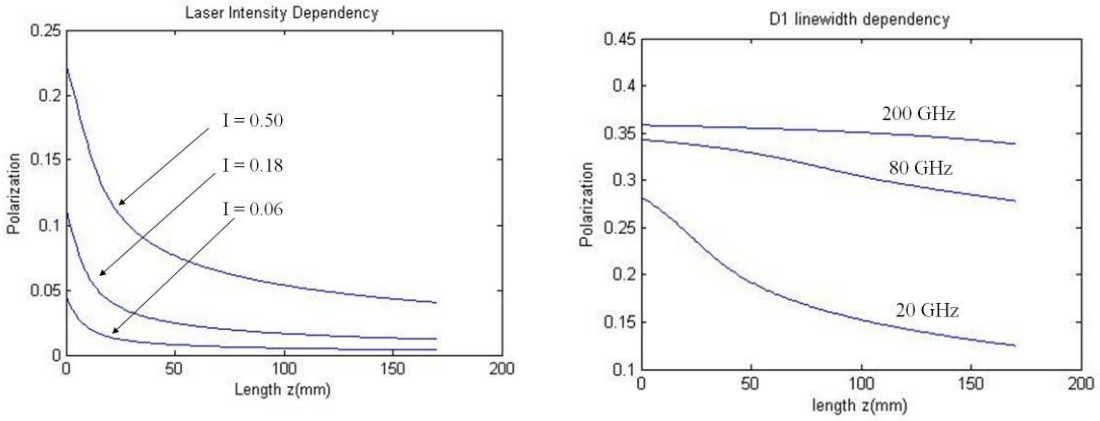

(a) (b)

Figure 2.8: (a) Polarization as a function of laser intensity, 0.06, 0.18 and 0.50 W/cm^2 (b) Polarization absorption bandwidth dependency, 20, 80 and 200 GHz.

xenon perfusion as a free magnetic tracer. With some modifications for the magnetic behavior in the Ketty-Schmidt equation we have:

$$\frac{d}{dt}M_T(t) = FM_A - (\frac{F}{\lambda} + \frac{1}{T_1})M_T(t) \tag{2.4}$$

where M_T is magnetization in tissue, M_A magnetization in arteries, F is blood perfusion to tissues, and λ_{bt} is the blood tissue partition function. The solution to this

equation is the convolution integral.

$$M_T(t) = \int_0^t F M_A e^{-(\frac{F}{\lambda}+\frac{1}{T_1})(u-t)} du \tag{2.5}$$

Constant flow mode - In the first approximation we assume the arterial input function is constant. Then the convolution integral can be written as:

$$M_T(t) = F M_A \int_0^t e^{-(\frac{F}{\lambda}+\frac{1}{T_1})(u-t)} du \tag{2.6}$$

and the solution to this equation is:

$$M_T(t) = \frac{F M_A}{\frac{F}{\lambda}+\frac{1}{T_1}}(1 - e^{-(\frac{F}{\lambda}+\frac{1}{T_1})t}) \tag{2.7}$$

Magnetization in tissues can be sampled using MRI. If the arterial input function and the relaxation map are known, the equation can be solved numerically for perfusion flow. In addition to the abovementioned decay processes, xenon magnetization decays as a result of applied RF pulses. After each RF pulse the remaining magnetization will be:

$$M_T^i(t) = \frac{F M_A}{\frac{F}{\lambda}+\frac{1}{T_1}}(1 - e^{-(\frac{F}{\lambda}+\frac{1}{T_1})\tau})(e^{-(\frac{F}{\lambda}+\frac{1}{T_1})\tau} cos(\alpha)^i) sin(\alpha) \tag{2.8}$$

where α is the tip angle. However, between this sampling and the next, tissues uptake more polarized xenon. In this case, the total magnetization will be the sum of fresh xenon magnetization and all magnetization from remaining xenon. After n sampling the magnetization will be:

$$M_T^n(t) = \frac{F M_A}{\frac{F}{\lambda}+\frac{1}{T_1}}(1 - e^{-(\frac{F}{\lambda}+\frac{1}{T_1})\tau}) \frac{1 - (e^{-(\frac{F}{\lambda}+\frac{1}{T_1})\tau} cos(\alpha))^n}{1 - e^{-(\frac{F}{\lambda}+\frac{1}{T_1})\tau} cos(\alpha)} sin(\alpha) \tag{2.9}$$

The system will reach the steady-state if polarized xenon is injected for a long time compared to the decay time constant. Also the number of RF pulses applied by the system at this point is assumed to be large. Then we have:

$$M_T^\infty(t) = \frac{F M_A}{\frac{F}{\lambda}+\frac{1}{T_1}} \frac{1 - e^{-(\frac{F}{\lambda}+\frac{1}{T_1})\tau}}{1 - e^{-(\frac{F}{\lambda}+\frac{1}{T_1})\tau} cos(\alpha)} sin(\alpha) \tag{2.10}$$

Figure 2.9a shows the magnetization as a function of tip angle for several perfusion flow rates. As can be seen, is sensitive to the flow rate. Again Figure 2.9b shows M_T as a function of tip angle for different values. Magnetization is a sensitive function of relation time, especially, at low tip angles. This dependency becomes much more insensitive as tip angle gets close to 90°.

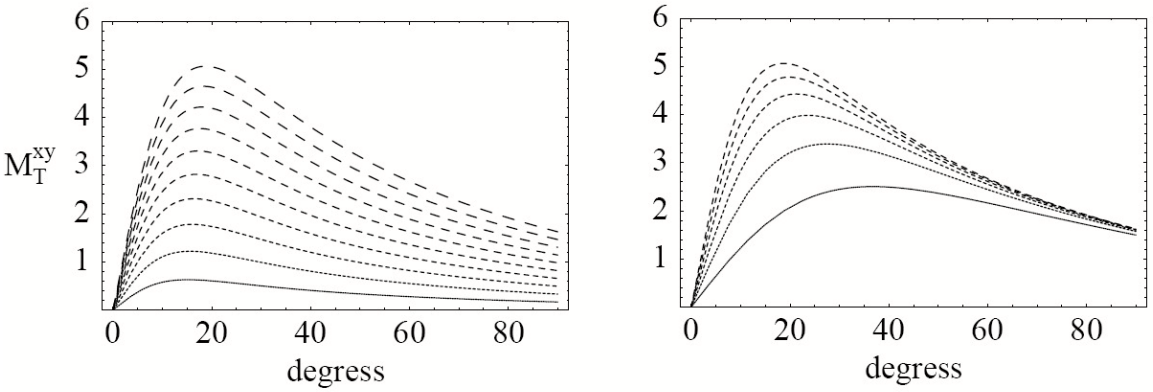

(a) (b)

Figure 2.9: (a) (Left) Magnetization as a function of flow. As flow increase the magnetization replacement rate increases. (b) (right) Magnetization as a function of relaxation time. As relaxation time increases the accumulated magnetization increases.

Including the depolarization, due to RFs, in the model, it can be written as:

$$M_n(t) = \sum_{n=1} (cos(\theta) e^{-\frac{t}{T_2^*}})^{(n-1)} \int_{(n-1)\Delta t}^{n\Delta t} C_a(\tau) R(t-\tau) d\tau \tag{2.11}$$

In equation refRF, C_a is the magnetization of the tracer in the arteries supplying the tissue. Magnetization is equal to the concentration of the tracer multiplied by its polarization at the time t.where n is the number of samples (images). Equation (2) after discretization can be approximated by:

$$M_n(t) = \sum_{n=1}^{N} (cos(\theta) e^{-\frac{t}{T_2^*}})^{(n-1)} C_a(n\Delta t) R(t - n\Delta t) \tag{2.12}$$

The perfusion model above can be expressed in the form of a linear matrix equation

as:

(2.13)

$$\begin{bmatrix} M(0) \\ M(\Delta t) \\ \vdots \\ M((n-1)\Delta t) \end{bmatrix} = \begin{bmatrix} C_a(0) & 0 & \dots & 0 \\ C_a(\Delta t) & (cos(\theta)e^{-\frac{t}{T_2^*}})C_a(0) & \dots & 0 \\ \vdots & \vdots & \ddots & \vdots \\ C_a((n-1)\Delta t) & cos(\theta)e^{-\frac{t}{T_2^*}}C_a((n-2)\Delta t) & \dots & (cos(\theta)e^{-\frac{t}{T_2^*}})^{n-1}C_a((0)\Delta t) \end{bmatrix} \times F \times \begin{bmatrix} R(0) \\ R(\Delta t) \\ \vdots \\ R((n-1)\Delta t) \end{bmatrix}$$

There are several methods to deconvolve the residue function from equation 2.13 Singular value decomposition is one of these methods.

To examine the technique's accuracy in low and high flow regimes, flow rates in the range of 10 to 60 ml/100gr/min were studied. Since noise is the main source of instability in the solutions of these integral equations, the stability and sensitivity of the resulting functions were investigated by setting the signal to noise ratio (SNR) to a set of different values between 10 and 100. The T_1 was assumed to be 4s in all of the simulations.

The data matrix was generated by sub-sampling the simulated tissue magnetization at a rate corresponding to actual imaging. The AIF was also sampled at the same rate and the values were implemented into the convolution matrix operator. To determine the flow rate and the residue function, equation 2.13 was deconvolved using SVD.

Figure 2.10a shows the calculated blood flows using the compensated and uncompensated models simulations of a low-angle imaging. Surprisingly, the flow rate

underestimations are similar among the results of compensated and uncompensated models. At a SNR of 100 and a flow range of 10 - 60 ml/100gr/min, the average flow underestimation was 14.9±0.5% .

Comparing the residue functions calculated by the two models, the results show that the uncompensated model underestimates the residue function and the MTT, since the MTT is proportional to the area under the residue function. This can be explained based on the aforementioned difference in working with magnetization rather than concentration. In the uncompensated model, the decrease in tissue magnetization is interpreted as a result of shorter transition time rather than depolarization, since this model cannot distinguish between the different sources of magnetization diminution. Figure 2.10b shows the estimated MTT-to-true-MTT ratio for the corresponding flow rates. The uncompensated model underestimates the MTT by 19.2±0.2%. Defining the relation between cerebral blood volume (CBV), CBF and MTT as:

$$CBF = \frac{CBV}{MTT} \tag{2.14}$$

as a result of an underestimation of both MTT and CBF, CBV will also be underestimated. The compensated model estimates the CBV with a good accuracy; however, it slightly overestimates the mean transition time. The overestimation was calculated 8.9±2.6% for short MTTs. As will be discussed later, regularization, as part of smoothening, prevents the fast decay of the estimated residue function in large ts that eventually results in an overestimation of the area under the curve. Figures 2.11 show the simulation results for perfusion related parameters at SNRs equal to 10 and 100. Although at high signal to noise ratios different regularization techniques show almost no advantage over each other, there is a clear disadvantage to using FOT instead of SOT and TSVD at low SNRs regularizations. At SNR =

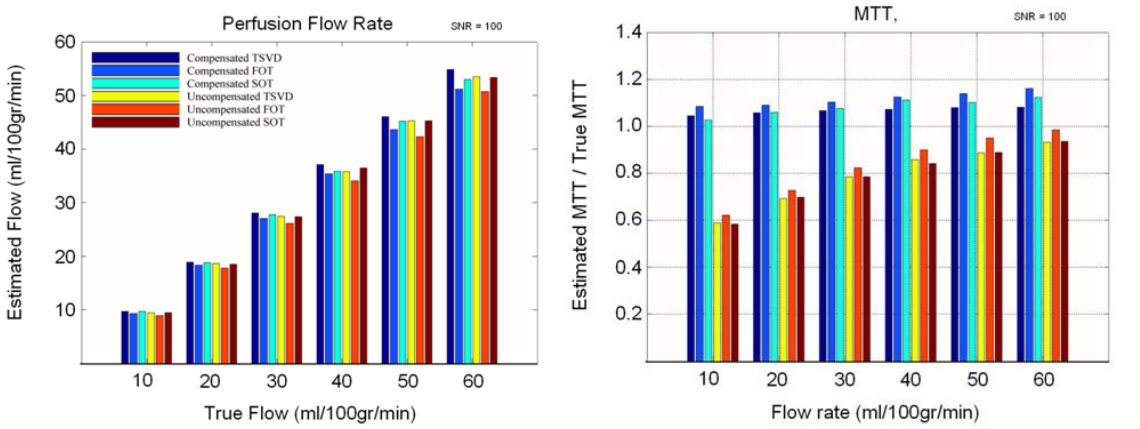

(a) (b)

Figure 2.10: (a) (Left) Estimated flow rates using TSVD, first order Tikhonov (FOT), and second order Tikhonov (SOT) regularization with and without consideration of the depolarization. (b) (right) Estimated MTT/true MTT for different flow rates, using compensated and uncompensated models.

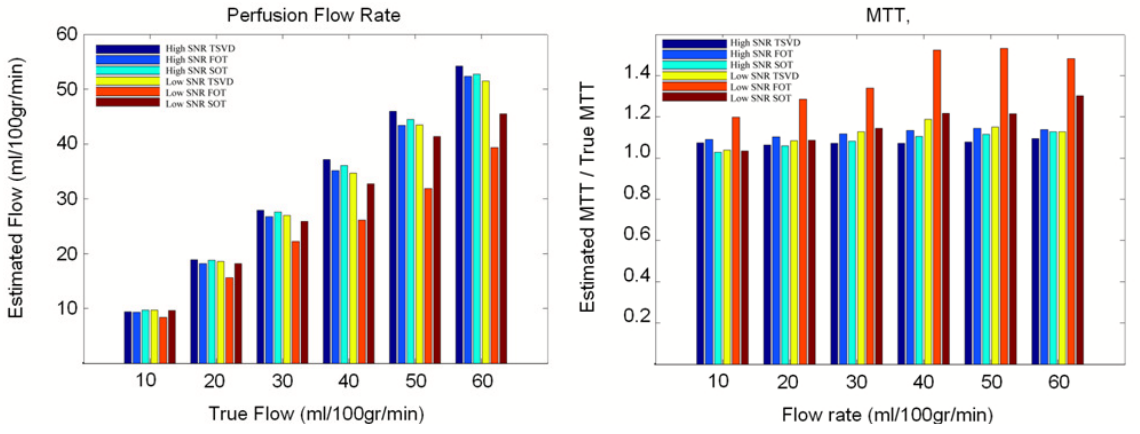

(a) (b)

Figure 2.11: (a) (left)The flow rate calculated using TSVD, FOT, and SOT regularizations at SNR =100 (High) and SNR =10 (Low). (b) (right)Normalized MTTs as a function of flow rates at high and low SNRs, using TSVD, FOT, and SOT regularizations.

10, the flow underestimations are 28.4% for FOT and 14.4% for SOT regularization. At the same signal to noise ratio MTT is overestimated by and , respectively, using FOT and SOT.

2.3 Conclusion

As mentioned before xenon is more than just a contrast medium. Much spectroscopic information can be extracted from its NMR signal. High signal to noise ratio, lack of background signal, large chemical shift, are among the advantages of using xenon over other current tracers. Some of the difficulties in perfusion measurements such as partial volume effect in AIF measurement and tracer recirculation can be easily avoided using xenon. At the same time, some major shortcomings with the polarized xenon perfusion measurement convinced us that in spite of all these advantages xenon perfusion measurement might never become a clinical procedure. Very short T_2^* in blood prevents fast imaging pulse sequences such as EPI. As we will show in the following high temporal resolution is required for the accurate flow estimation. Also, considering large amount of the polarization is lost on the way delivering the tracer to the brain tissue and later due to the applied RF pulses, a renewable source of polarized xenon will be required. To address this issue the continuous delivery was suggested (and simulated) which unfortunately does not resolve the issues completely. One objection to this approach is that since xenon is an anesthetic material which affects the blood flow, especially when the patient is exposed for a long time or to a high dose of xenon. Although polarized xenon might not be a great choice for the cerebral blood flow measurement, it is valuable method for cavity imaging purposes such as lung and lung perfusion imaging. Xenon has also applications in

functional cardio imaging, due to its high sensitivity to the presence/lack of oxygen in oxygenated/deoxygenated blood.

CHAPTER III

THEORY AND SIMULATIONS

As mentioned in the previous chapter, the extent of the ischemic tissue and the necessity of thrombolytic treatment can be determined based on the cerebral blood flow. The threshold of transition from a healthy tissue to an ischemic penumbra or a stroke core is sometimes only a few ml/100gr/min. Therefore diagnosis requires very precise measurements of cerebral blood flow. Thermal and systematic noise, bolus delay and dispersion are among major sources of error in flow quantification. To date, many mathematical approaches have been suggested to minimize the effects of these sources of error on the estimated flow rate. In the field of inverse problems, these mathematical methods, which improve the stability of the solutions, are referred to as "regularization methods". In this chapter we will review some of these regularization methods and we will compare them to our method, generalized Tikhonov. In the section III.1 the two original models of blood flow measurements by Kety-Schmidt and Meier-Zieler are introduced. In the section III.2 singular value decomposition (SVD) and maximum likelihood estimation (MLE) as two powerful mathematical methods for solving inverse problem are discussed. It can be mathematically proved that our method is supported by both SVD and MLE. In the other words, generalized Tikhonov formalism can be derived from the either of these two

methods. Different types of regularization, including Truncated SVD and Tikhonov, as well as the limitations of flow calculation in ill-posed problems are investigated in section III.3 as well. Then, in section III.4, generalized Tikhonov regularization will be introduced and its sensitivity to noise, delay and dispersion, will be compared to the previously mentioned regularization methods. In the last section, I conclude with the advantages and disadvantages of the new method.

3.1 Perfusion Models

Blood flow can be measured using any model that correlates a measureable dynamic parameter of a tracer to the blood flow. Almost all perfusion models are originated from the two original models, Kety-Schmidt model [28], for diffusible tracers, and Meier-Zieler [46], [57] model, for non-diffusible ones. The first model estimates the flow rate based on the change of the tracer magnetization in the tissue and the second method which is based on the indicator - dilution theory uses concentration-time curve of the tracer as the dynamic parameter of the model.

3.1.1 Kety-Schmidt Model

The Kety-Schmidt model is derived from Fick's first law $J = -D\frac{\partial \phi}{\partial x}$ where "J" is the diffusion flux, "D" is the diffusion constant and "ϕ" is the concentration. In biological perspective this equation gives rise to the equation:

$$F = -P \times A(C_2 - C_1) \tag{3.1}$$

where P is the permeability, A is the surface between the two media and the last term represents the concentration difference. In this model a diffusible tracer is introduced to the tissue through blood circulation.C_T is the concentration of the

tracer in the tissue per unit mass of the tissue (this unit is usually 100 grams of the tissue). The concentration per volume blood, are expressed by C_A in the supplying artery and by C_V in the draining vein, respectively. Based on Fick's first law the tissue concentration flux and the other two concentrations are related as:

$$\frac{dC_T}{dt} = F(C_A - C_V) \tag{3.2}$$

where F is the flow rate which is expressed in ml/100gr/min. Kety and Schmidt assumed that the equilibrium is instantaneous. The partition coefficient, the ratio of the concentration of a component in a two compartment medium, is assumed constant. Partition coefficient can be expressed as the ratio of the tracer concentration in the venous blood and that in the tissue:

$$\frac{C_V}{C_T} = \lambda \tag{3.3}$$

Replacing C_V in equation 3.2 with equation 3.3 we will have:

$$\frac{dC_T}{dt} = F(C_A - C_T/\lambda) \tag{3.4}$$

In the presence of polarization relaxation, polarization decay needs also to be added to the equation 3.4 which results only that part of the signal which participates in MR (magnetization) to be considered:

$$\frac{dM_T}{dt} = F(M_A - \frac{M_T}{\lambda}) - \frac{M_T}{T_1} \tag{3.5}$$

This equation has an analytical solution:

$$M_T(t) = F \int_0^t M_A(t-\tau) e^{(-\frac{F}{\lambda} + \frac{1}{T_1})\tau} d\tau \tag{3.6}$$

We used this equation in chapter II to calculate the effect of RF pulses on perfusion-related parameters.

3.1.2 Meier-Zieler

In this model, it is assumed that the entire injected tracer stays in the vasculature and is not capable of diffusing into the tissue. Also, it is assumed that h is the distribution of the travel time for the tracers in the tissue. The residue function or the instantaneous fraction of the tracer in the tissue, also called as residue function, is expressed as:

$$R(t) = \int_0^t (1 - h(\tau))d\tau \tag{3.7}$$

This can also be considered as the tissue response to arterial concentration, C_A, which we will refer to as the arterial input function (AIF). This concentration is related to C_V through a convolution equation:

$$C_T = F \int_0^t C_A(\tau - t)R(\tau)d\tau = F(C_A \otimes R) \tag{3.8}$$

The residue function is a non-increasing function (i.e. constant or decreasing). Assuming the tracer cannot leave the tissue in an infinitely small time, residue function can be considered equal to one at the initial moment (R(0)=1). This is an important characteristic of residue functions, which as we will show later in this chapter, is required to estimate the flow rate.

3.2 Residue Function Deconvolution

As mentioned above, to calculate the blood flow, the residue function needs to be deconvolved from the tissue signal C_T. As yet, many different parametric and non-parametric deconvolution methods have been investigated [46, 10]. Singular value decomposition (SVD), Fourier transformation-based (FT) method, Gaussian process

deconvolution (GPD), iterative blind deconvolution [21] and Bayesian estimation method are among them. Almost all of these methods can be categorized under two major headings: Singular value decomposition and maximum likelihood estimation [11] which both will be introduced in this chapter. Both of these two methods are derived from least square methods.

3.2.1 Singular Value Decomposition

Singular value decomposition is a factorization method which is used widely in linear inverse problems. The principle idea in this method is that every matrix G can be factorized to three matrices, U, S and V [18].

$$G_{m\times 1} = U_{m\times m} S_{m\times n} V^{\dagger}_{n\times n} \tag{3.9}$$

U and V are orthogonal matrices which span the data and model spaces, respectively. S is a diagonal matrix with all positive singular values in a descending order on its diagonal. In a linear equation:

$$d = Gm \tag{3.10}$$

The factorized G:

$$G = USV^{\dagger} \tag{3.11}$$

can be used to calculate the pseudo-inverse of G as:

$$G^{\#} = VS^{\#}U^{\dagger} \tag{3.12}$$

where $S^{\sharp}$ is the matrix S matrix with its non-zero diagonal elements inversed. This pseudo-inverse matrix can be applied to the equation 3.10 to calculate the model m as:

$$m = G^{\#}d \tag{3.13}$$

It can be shown that the model calculated using this method is also the least square solution to the equation 3.10. As mentioned above SVD is a powerful method for linear inverse problems, however, the perfusion model is a nonlinear convolution equation. This problem can be resolved when the equation is rewritten as [52]:

(3.14)
$$\begin{bmatrix} c(0) \\ c(1) \\ \vdots \\ c(m-1) \end{bmatrix} = F \begin{bmatrix} AIF(0) & 0 & \dots & 0 \\ AIF(1) & AIF(0) & \dots & 0 \\ \vdots & \vdots & \ddots & \vdots \\ AIF(n-1) & AIF(n-2) & \dots & 0 \end{bmatrix} \begin{bmatrix} R(0) \\ R(1) \\ \vdots \\ R(m-1) \end{bmatrix}$$
$$= F(G_{m\times n} \times r_{n\times 1})$$

where c is the concentration at the tissue and R is the residue function. The solution to this equation is:

(3.15)
$$F.r\,(t) \cong F \begin{bmatrix} R\,(0) \\ R\,(1) \\ \vdots \\ R\,(n-1) \end{bmatrix} = G^{\#}_{n\times m} \times \begin{bmatrix} c\,(0) \\ c\,(1) \\ \vdots \\ c\,(m-1) \end{bmatrix}$$

Considering R(0)=1, flow can be calculated as $F \times R(0) = F$.

3.2.2 Maximum Likelihood Estimation

MLE is a statistical method which can be used in model fitting and parameters estimation. It is assumed that a group of probability distributions functions, with density functions such as f_m, exists that describes the distribution of the parameters of the model m. For a gives data set $d = x_1, x_2, \ldots$, and the density function f_m the probability that the model generates results which are similar to the data, can be

expressed as:

$$q(m \mid d) = f_m(d \mid m)p(m) \tag{3.16}$$

If more data sets are available this equation should be replaced by:

$$Q(m \mid d) \propto f_m(d_1 \mid m)f_m(d_2 \mid m)\ldots f_m(d_n \mid m) \tag{3.17}$$

The concept of MLE is to find the set of model parameters that gives the best fit to the data. This formalism can be written in terms of covariance matrices of the data and the model. Then SVD is used to calculate the model that maximizes the probability. As mentioned before, this method is also a variation of least square methods. The major difference between this method and SVD based methods is that MLE gives a distribution of the most probable model parameters instead of the parameters themselves. However, the mean of the values can be used as the model parameters.

MLE is an iterative method. Each step applies more restricted constrains on the distribution of the parameters. However, to have results with a tight distribution we need to make strong assumptions on the initial distribution. Vonken et. al. used the standard form of this least square method in dynamic susceptibility contrast cerebral blood flow estimation. This study showed some sensitivity to the discretization of arterial input function [53]. The other disadvantage of the method was lack of a clear criterion for the optimum stop-point for the iteration. Both of these problems were corrected, to some extent, by Williats and her colleges who introduced a criterion for the optimum step to stop the iteration, also, they improved sensitivity issue by using interpolation [55]. However, there are still a few disadvantages with this method. For example, the linear interpolation, is not a proper method when the temporal resolution is low. In terms of computation, a large number of iterations is usually

needed if the high frequency terms are of interest.

3.3 Regularization

Regularization refers to mathematical methods which improve the stability in such problems. Perfusion measurement using the indicator-dilution model is an ill-posed problem in the Hadamard sense which has roots in fast decay of singular values and the nontrivial data and model null spaces. Most of the Fredholm integral equations of the first kind (IFK) are ill-posed. That causes sensitivity to noise and instability in the solutions. The singular matrix S, (the equation3.9) in most of such problems, is in the form of:

$$S_{m\times n} = \begin{bmatrix} S_{p\times p} & 0 \\ 0 & 0 \end{bmatrix} \tag{3.18}$$

In the presence of zeros in singular values, either a nontrivial null model space exists and the solution is not unique or the solution is the least squares solution projected on the subspace spanned by G. In such cases the solution is not unique which means the equation is not well-posed according to the Hadmard conditions [22]. Such problems are very sensitive to noise. The effect of noise on high frequency terms is always more noticeable. Regularization methods either act as a low-pass filter or try to reconstruct the high frequency terms by relying on a priori information (curve fitting). In the following, truncated SVD and Tikhonov regularization, two powerful regularization methods, are introduced and their effect on ill-posed problems will be studied.

3.3.1 Truncated singular value decomposition

As mentioned above, small singular values give rise to the ill-posed condition in inverse IFKs. Since the major part of signal is in the low frequency domain and terms corresponding to high frequencies are small, this part of the spectrum receives more relative impact from the noise in the system. To show this mathematically let's study the SVD solution to a least square function in the form of:

$$\| d - Gm \|_2^2 \tag{3.19}$$

Which can be expressed in terms of matrices U, S and V as :

$$m = \sum_{i=1}^{n} \left(\frac{U_i^{\dagger}.d}{S_i} \right) V_i \tag{3.20}$$

Again, it can be seen that as $S_i \rightarrow 0$ the term $\frac{(U_i^{\dagger}.d)}{S_i}$ diverges unless the numerator goes toward zero as well. For small singular values, the corresponding U_i is a rapidly oscillating vector. In the absence of noise, $U_i^{\dagger}.d$ decays to zero, usually, faster than S_i. In the presence of noise this condition is not usually satisfied. This results in the instability of the solutions which appears as oscillation in the results. One approach to overcome this instability is to truncate the terms corresponding to high frequencies, or equivalently, to small singular values. Truncation threshold in SVD problems is the lower limit for singular values which are preserved. Now, the question is what the truncation threshold value should be. The larger the truncation threshold is the more stable the solution will be. However, with higher threshold there will be more information lost. The choice of threshold maybe a function of signal to noise ratio. In our particular case, blood flow estimation, discarding high frequency terms results in underestimation of the flow. In the other words, the higher the threshold, the more underestimation. Figure 3.1 shows the residue function calculated using

SVD and TSVD with thresholds equal to 0.1 and 0.2 of the maximum singular value for SNR = 20.

Andersen et al. used a method suggested by Liu et al. to find the optimized threshold. They showed that is only beneficial if the residue function is exponential [3]. Lack of a criterion for finding the optimum threshold value is a major flaw for this method.

3.3.2 Tikhonov Regularization

The second approach, called Tikhonov regularization, regularizes the solution by applying a restriction on the model or its derivatives. Zero, first and second order Tikhonov smooth the zero, first and the second derivative of the model, respectively. This type of regularization is a proper choice for perfusion model's residue functions since these functions are naturally smooth and free of sharp peaks. In the general form, Tikhonov regularization finds the solution:

$$\| d - Gm \|_2^2 + \alpha^2 \| L_i m \|_2^2 \tag{3.21}$$

α is the regularization parameter. L_i is the Tikhonov matrix which is a unitary matrix for the zero order Tikhonov and

$$L_1 = \begin{bmatrix} 1 & -1 & 0 & \dots & 0 & 0 \\ 0 & 1 & -1 & \dots & 0 & 0 \\ 0 & 0 & 1 & \dots & 0 & 0 \\ \vdots & \vdots & \vdots & \ddots & -1 & 0 \\ 0 & 0 & 0 & \dots & 1 & -1 \end{bmatrix} \quad L_2 = \begin{bmatrix} 1 & -2 & 1 & \dots & 0 & 0 \\ 0 & 1 & -2 & \dots & 0 & 0 \\ 0 & 0 & 1 & \dots & 0 & 0 \\ \vdots & \vdots & \vdots & \ddots & 1 & 0 \\ 0 & 0 & 0 & \dots & -2 & 1 \end{bmatrix} \tag{3.22}$$

for the first and the second order Tikhonov matrices, respectively. Regularization parameter - At high signal to noise regime the first term of the equation is very small compared to the second term. This means that the residual error is close to

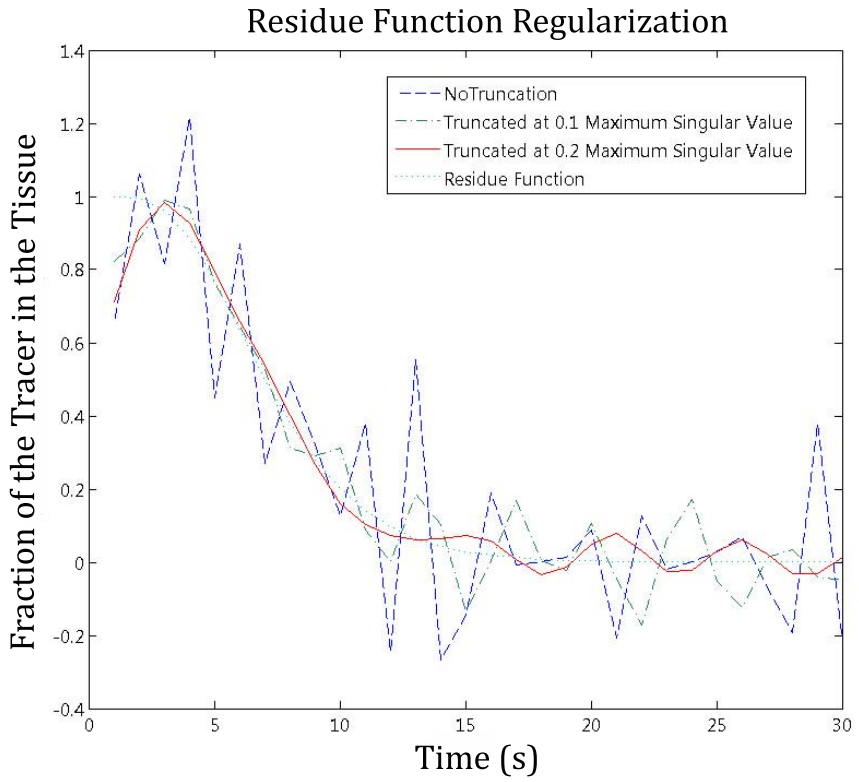

Figure 3.1: Calculated residue function form simulated data using TSVD. No truncation, truncated at 10% and 20% of the maximum singular value. The signal to noise ratio is 20. Oscillations decrease as the threshold increases.

zero, when the norm of the model or its derivatives is not. This makes the influence of the second term dominant over the first term and since the tendency in regular Tikhonov is to decrease the model or its derivatives toward zero, the estimated model has lower curvature compared to the true model. In the low signal to noise regime, the scenario is opposite. The first term is the dominant one and that prevents the second term from the smoothing the model. The regularization parameter is a Lagrange multiplier that at its optimum value equalizes the participation of either of the two terms. In our simulations, we tried the two popular approaches, L-curve and generalized cross validation, to find the optimum regularization parameters. We will review some of advantages and disadvantages of them in the following.

L-curve criteria - There are many different methods to find the optimum regularization parameter of the equation 3.21. L-curve is probably the simplest and the most popular method for this purpose. In this method the norm of the residue function ($\| f.G \times r - c \|$) is plotted vs. the norm of the regularization term $\| L(r - r_0) \|$ on a log-log scale.

The curve usually has L-shape appearance and shows the trade-off in the simultaneously minimizing the two terms of the equation. The corner of the curve gives the optimum regularization parameter in regard to the minimum compromise in the trade-offs. Johnston and Gulrajani have shown that in the presence of large correlated noise, L-curve, at least with its current criteria in finding the corner of the curve based on the maximum curvature, is not a beneficial technique [29]. This criterion fails since no clear corner exists when the correlated noise exceeds the random noise.

Generalized cross validation criteria - The other method of finding the optimum regularization parameter is known as generalized cross validation method. In this approach the criteria of optimization is choosen to be the best re-prediction of miss-

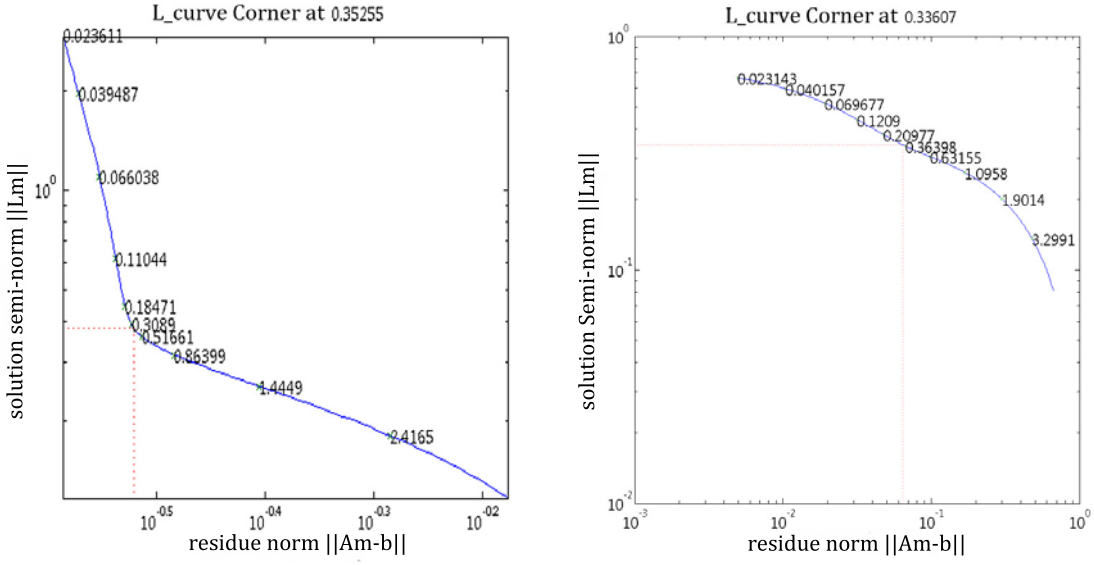

(a) (b)

Figure 3.2: (a) L-curve for a first order Tikhonov problem. SNR = 10 (b) L-Curve at SNR = 1000. No corner exists when systematic correlated noise exceeds thermal white noise.

ing data. In this method, using a subset of data points, the residue functions for different values of the regularization parameter are calculated.

$$\| d^{(i)} - Gm^{(i)}_{\alpha,L} \|_2^2 + \alpha^2 \| Lm^{(i)}_{\alpha,L} \|_2^2 \tag{3.23}$$

where $m^i_{\alpha,L}$ is the solution to the equation when $d^i$is missing. Then the $m^i_{\alpha,L}$ is used to reproduce the data. This process is repeated for every data point in the data set. The optimum regularization value would be the one that minimizes the average residual norm of the reproduced data and the original data. One problem with cross validation is that it is computationally expensive. It becomes more important when it is used for finding the regularization parameter in a high resolution model. To overcome this problem we used the approximation which is m times faster than the conventional method:

$$V(a) \simeq \frac{m \| f.G \times r_{a,L} - c \|^2}{Tr(I - GG^{\#})^2} \tag{3.24}$$

In the above equation V is the residual norm and m is the size of the residue matrix.

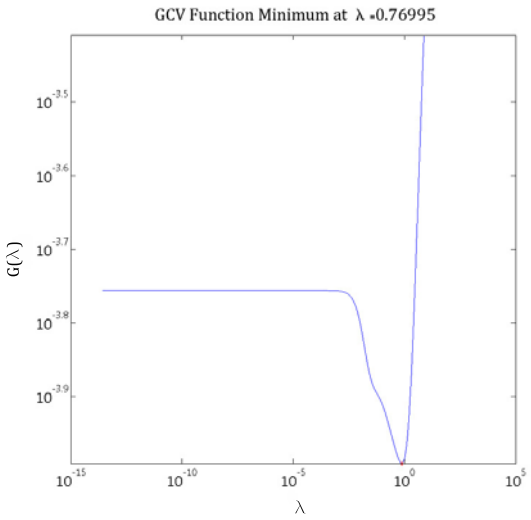

Figure 3.3: GCV curve. The minimum shows the optimum regularization value. SNR = 10

The simplification was done under the assumptions:

$$\lim_{x \to +\infty} \| f.G \times r_{a,L} - c \|_2^2 \quad \to 0 \tag{3.25}$$

Since the size of the residue function is fixed and finite, this assumption is not completely valid and the equation 3.24 is only an approximation of the cross validation method. However, in our simulations we found the regularization parameters calculated with both approaches are very close in all noise regimes. As Hansen [24] and O'leary [45] have poited out, the other disadvantage of GCV, is that it usually mistakes the correlated noise for part of the signal. Our experience with CGV also confirms a similar problem.

3.4 Generalized Tikhonov Regularization

As mentioned before the solution to the Tikhonov regularization minimizes the equation:

$$\| c - f.G \times r \|_2^2 + \alpha^2 \| L \times r \|_2^2 \tag{3.26}$$

The first order Tikhonov matrix can be considered as an equivalent to the first order derivative operator in continuous domain. Minimizing the second term in the equation implies the assumption that the first derivative of the true model is zero or:

$$\frac{\partial R_{true}(t)}{\partial t = 0} \tag{3.27}$$

Clearly, this assumption is not accurate. As we mentioned before, residue function is a non-increasing function so:

$$\forall t \in (0, \infty); \frac{\partial R(t)}{\partial t} \leq 0 \tag{3.28}$$

Other orders of Tikhonov regularization are also built based on similar misassumptions. One consequence of this misassumption is flattening of the residue function that participates in the flow underestimation. What we expect from the regularization is to minimize the oscillations with causing a minimal underestimation. To achieve this goal we suggested a generalized form of Tikhonov regularization to minimize the oscillation/deviation of the estimated residue function from the expectation value of the model. This can be expressed mathematically as:

$$\begin{gathered} \| c - f.G \times r \|_2^2 + \alpha^2 \| r - \bar{r} \|_2^2 \\ \| c - f.G \times r \|_2^2 + \alpha^2 \| L \times (r - \bar{r}) \|_2^2 \end{gathered} \tag{3.29}$$

The above equations show the zero and first order generalized Tikhonov. From now on, we refer to this approach as first order generalized (FOG) Tikhonov. We will show that the new regularization improves the flow estimation accuracy. It is less sensitive to delay and dispersion when it is fed with the correct expectation residue function. Also, it reconstructs the actual shape of the residue function more accurately than the other methods.

3.4.1 Expectation value model

To use equations 3.29.a and 3.29.b, one needs to calculate the expected value of the residue function first. In the following a statistical model for this calculation will be presented. At this point we review some of the characteristics of residue functions. These characteristics can be used as prior information to estimate residue functions:

$$R(0) = 1; \lim_{t\to\infty} R(t) \to 0 \qquad \frac{\partial R(t)}{\partial t} \approx 0 \ \textit{when}\ t \leq \epsilon_1, \epsilon_2 \geq t \tag{3.30}$$

The first two conditions in equation 3.30.a were explained earlier in this chapter. The first condition implies that the whole tracer is in the tissue at the initial moment. Second condition implies that the tracer will be eventually completely washed out of the tissue. Conditions mentioned in equation 3.30.b are the more realistic forms of conditions in 3.30.a. They indicate that a minimum transition time, ϵ_1, exists for the tracer to pass through the tissue. In the other words, the probability of passage of the tracer through the tissue, in times shorter than ϵ_1, is almost zero. Also the major part of the tracer leaves the tissue in a finite time, ϵ_2. It can be shown that the tracer's travel through capillary network is a Poisson process. Let's assume that the tracer is composed of infinitely small elements and these elements travel through the imaging voxel (through every possible capillary pathway). The distribution of the travel time for such trips can be expressed in the form of a gamma distribution.

$$P(t; a, \theta) = \frac{t^{a-1} e^{-\frac{t}{\theta}}}{(\Gamma(a)\theta^{(} - a))} \tag{3.31}$$

where θ is the average time spent in each capillary. Based on this distribution the residue function can be calculated as:

$$R(t; a, \theta) = 1 - \int_0^t P(\tau; a, \theta) d\tau \tag{3.32}$$

To estimate $\bar{r}$, the initial value of the two parameters of the equation 3.32 , a_0 and θ_0, are estimated from the residue function calculated using TSVD:

$$\bar{r}_0 = \begin{bmatrix} R(0, a_0, \theta_0) \\ R(\Delta t, a_0, \theta_0) \\ \vdots \\ R((n-1)\Delta t, a_0, \theta_0) \end{bmatrix} \tag{3.33}$$

Although the estimated $\bar{r}$ might deviate from the true model, it is still much closer to the true expectation model than $r_0 = 0$, used in first order regular Tikhonov. Also, it carries the a priori information that the residue function is a non-increasing function. Now, using this expectation value of the residue function, equation 3.29 can be solved for the new residue function.

3.5 Simulations

Bolus tacking was simulated using MATLAB. In this simulation a gamma AIF is convolved with a residue function to create a tissue signal. The residue function is generated from one of the gamma, Gaussian, exponential or rectangular (box) distribution functions using equation 3.7. In future we will refer to this function as the true residue function. Using T_1, T_2 and the relaxivity constant, the program creates the AIF, the tissue signal and the system matrix. To minimize the discretization error, all the functions are generated with high resolution (< 256 points) and then are sub-sampled according to the desired TR. To simulate the thermal noise, white Gaussian noise is added to the data. In the other words, system matrix is always created from noise free AIF. This is not an unrealistic assumption since the signal to noise ratio of AIFs, due to much larger volume of blood in arteries than tissues, is

always much higher than the SNR of tissue signals. Simulations were used to compare the generalized Tikhonov regularization, the regular Tikhonov and the truncated SVD and investigate their accuracy in blood flow estimation. Also, the sensitivity to thermal and systematic noise, as well as, delay and dispersion were examined.

3.5.1 Blood Flow Estimation

May be the largest concern in the using generalized Tikhonov is the accuracy and the applicability of this method when the true residue function deviates from the gamma-based model residue function. To purely compare the two model-free methods to the generalized Tikhonov, several sets of delay and dispersion free tissue signals were generated. Data sets included flow rates from 10-100 ml/100gr/min. Simulations were repeated for signal to noise ratios equal to 5, 10 ,30 and 100. TR was set to 1s per image. Table 3.1 shows the results which showed, even in the presence of deviation from the true distribution, generalized Tikhonov can estimate the flow rate, if not more, as accurate as the other two regularization methods. Gamma, Gaussian and exponential distributions were used in residue function generation for this simulation. Results revealed a large difference in estimated flows at low SNRs between TSVD and regular Tikhonov. This can be explained based on the misassumption in regular Tikhonov mentioned previously. It becomes more significant in low SNRs because the regularization parameter is larger in the low SNR regime and that gives rise to the more participation of the second term of the equation.

In these simulations Generalized Tikhonov showed very promising. It is almost as stable as TSVD over the whole signal to noise spectrum which can be explained based on that the generalized Tikhonov residue model is supplied by TSVD. The estimated flow rates are also very similar among these two methods which means that the underestimation in regular Tikhonov has been corrected in the generalized method. In

the other words, Generalized Tikhonov has inherited all strong features of TSVD including more accuracy in flow estimation as well as more stability in different noise regimes. Comparing the smoothness of the functions, in figure 3.4, TSVD, in spite of truncation at 20% of the maximum singular value, still shows some oscillations. Also, the figure clearly shows that the slope reduction in regular Tikhonov which as mentioned before is a consequence of the misassumption. Generalized Tikhonov preserves the true residue function characteristics much better than the two others methods.

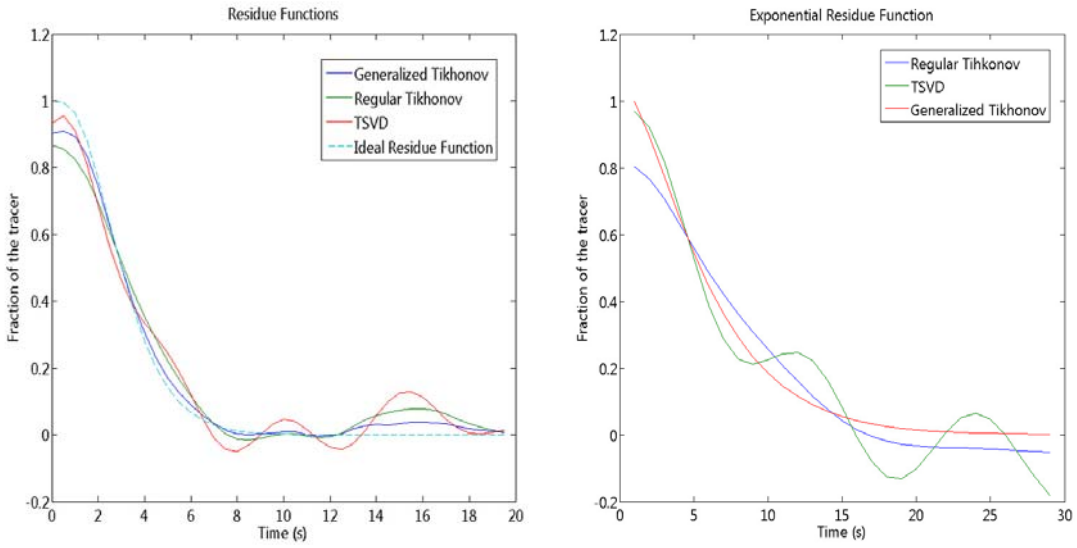

(a) (b)

Figure 3.4: (a) gamma (b) exponential based residue function estimated using TSVD, regular and generalized Tikhonov.

The interesting point is the considerable underestimation (20-23%), by all three methods, when the true model is an exponential residue functions. Exponential residue functions decay faster than other residue function over time. That points out the sensitivity of all three methods to fast decay of residue functions. Very similar situation can happen to any type of residue function when the imaged tissue

has a short mean transition time.

3.5.2 Mean Transition Time

Figure 3.5 shows the blood flow calculated for three different mean transition times. We chose to have high signal to noise ratio to make sure underestimations are purely caused by MTT. Simulations confirmed our previous results. The underestimation increases with decrease in the MTT. When MTT = 1s, underestimation was around 35%. At long MTT regime all three methods estimated flow rates close to 100% accurate. The very small underestimation by generalized Tikhonov can be explained base on that this method is biased and the other two are not (or at least not as much as this method is). One approach to overcome this problem is to increase the temporal resolution of the model by interpolation of the system matrix. As we will show later, unfortunately, this pushes the perfusion problem toward rank-deficiency without any increase in the model resolution in TSVD regularization. In low temporal resolution the systematic noise may even surpasses the thermal error in the system. Low signal to noise ratio results in larger error bars and adds to the uncertainty in the results. To keep the image informative and useful in diagnosis, higher spatial resolutions are desirable. However, as we'll study that in more detail, when interpolation is used in Tikhonov regularization the story is completely different and Tikhonov actually benefits from interpolation.

3.5.3 Temporal Resolution and Interpolation

In Imaging lower spatial resolution signal to noise ratio is the price one should pay to increase the temporal resolution. Now the question is in this tradeoff which one is more important. Lack of sufficient temporal resolution, results in large discretization error that may even surpasses thermal error in the system. Low signal to noise ratio

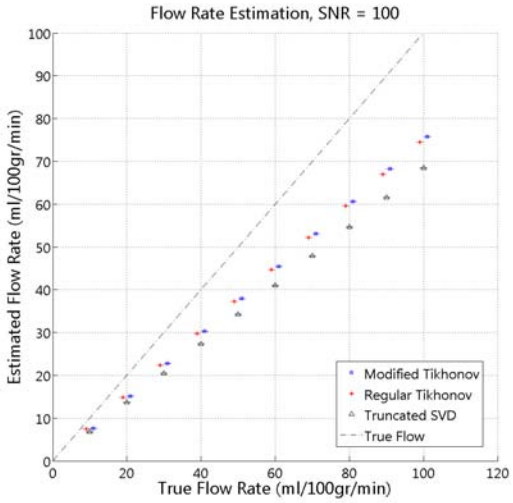

(a)

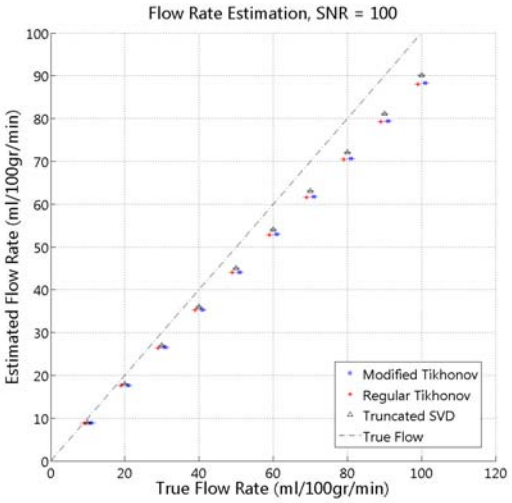

(b)

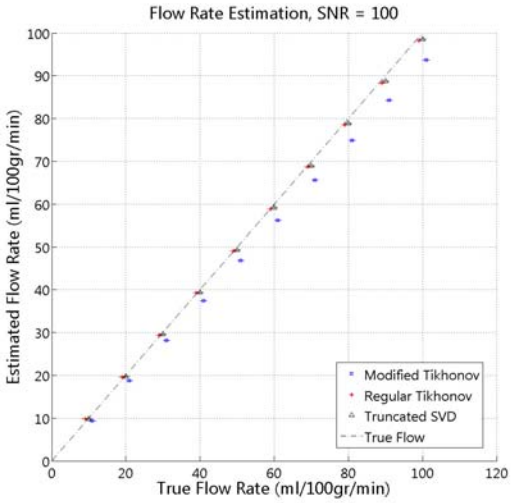

(c)

Figure 3.5: Flow estimation for different values of mean transition time. (a) MTT = 1s (b) MTT = 3s, (c) MTT = 6s. Underestimation decreases by the increase in the mean transition time.

results in larger error bars and adds to the uncertainty in the results. To keep the image informative and useful in diagnosis, higher spatial resolutions are desirable. Systematic noise, caused by limited sampling resolution, just similar to the thermal

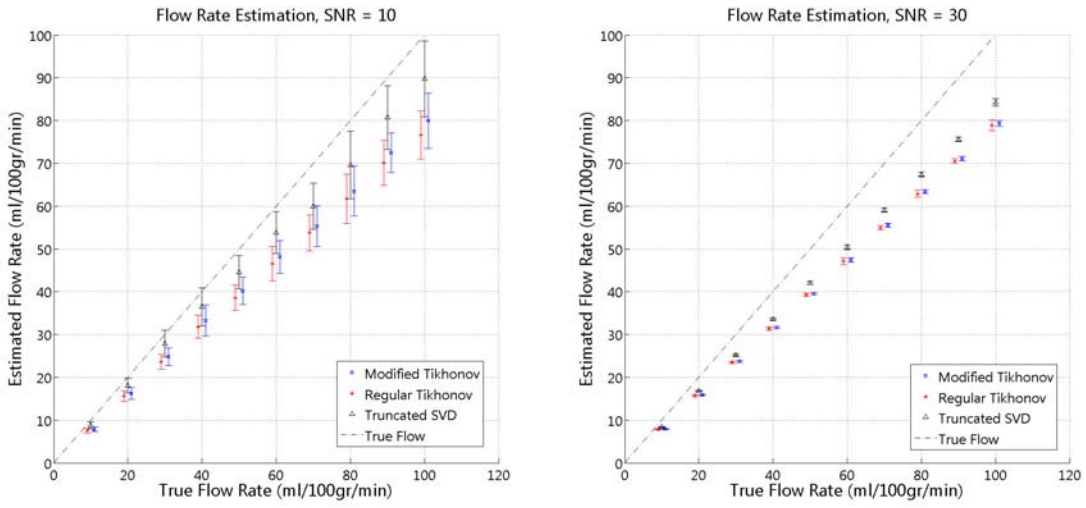

(a) (b)

Figure 3.6: increase in underestimation as a result of low temporal resolution. (a) SNR = 10 (b) SNR = 30.

white noise, results in flow underestimation. To study the effect of TR on the flow rate the flow measurement was simulated with doubled TR (TR = 2s). TSVD showed less sensitive than the Tikhonov regularizations to the lower temporal resolution which resulted 8-12% reduction in the estimated flow by Tikhonov regularizations. To study the effect of interpolation, low resolution system matrices were interpolated and up-sampled to the same model resolution as previous simulations. The rows of the system matrix, which determine the model resolution, were interpolated using 2D Cubic spline interpolation method which we believe has. Spline interpolation is a form of piecewise polynomial interpolation. Spline interpolation is preferred over polynomial interpolation because the interpolation error can be made small even when using low degree polynomials for the spline. As figure 3.7 shows the

underestimation in generalized Tikhonov regularizations was restored back to the original values. This improvement is more significant in generalized Tikhonov than the regular Tikhonov regularization. One reason for that is that l-curve overestimates the optimum value for the regularization parameter, when the number of rows and columns are close. That results in the dominancy of the Tikhonov matrix which as mentioned before results in flattening and underestimation of the flow rate.

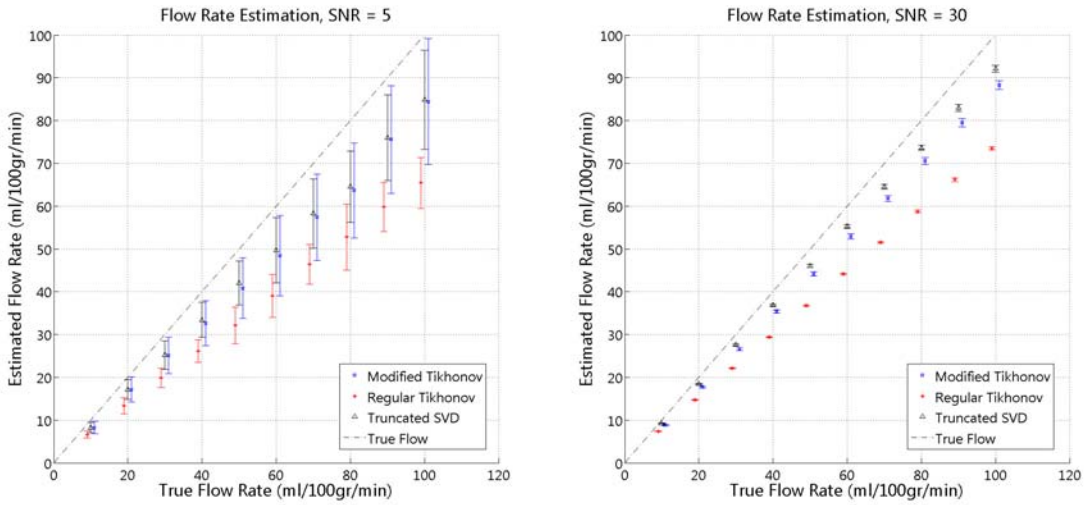

(a) (b)

Figure 3.7: Underestimation reduction using interpolation. (Left) SNR = 10 (right) SNR = 30.

3.5.4 Rank-deficiency and the Model Resolution

As mentioned before, in TSVD, using interpolation moves the system matrix toward rank deficiency which the first consequence of that is that the solution will not be unique anymore. Also, absolute zeros in the singular values make the inverse problem more vulnerable to instability in the presence of noise. Figure 3.8 shows the singular values in an original system matrix vs. those in the interpolated one. Half of the singular values of the double sampled matrix are absolute zeros. The rank of the matrix as a measure of its resolution tells us that interpolation does not increase the resolution. However, previous results showed, it does reduce the systematic error

which implies that the systematic error and lack of sufficient temporal resolution are not exactly equivalent. The ratio of the largest to the smallest non-zero singular value can be used as a measure of the stability of the system. That ratio for our sample matrix here is in the range of 20-30 which implies that the system is rather stable. The resolution matrix of the system matrix is defined as:

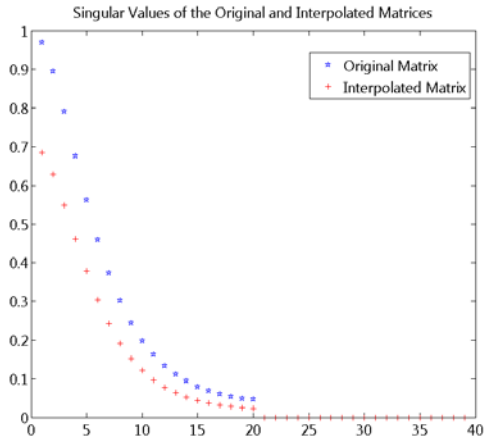

Figure 3.8: Singular values in the original system matrix vs. the interpolated matrix. The rank of the both matrices is the same which makes the interpolated matrix rank-deficient.

$$R_m = G^{\#}G = V_p V_p^{\dagger} \tag{3.34}$$

In a full rank matrix, resolution matrix is supposed to be a unitary matrix. Deviation from unitary matrix can be used as an indicator of the extent of the null model space. Figure 3.9 shows the resolution matrices and their deviation from the unitary matrix for the original and the interpolated system matrices. The resolution matrix in the interpolated matrix shows some deviation from the unitary matrix. Our simulations show that the width of the non-zero diagonal terms is a function of the ratio of the size of the interpolated matrix to the original one. In the other words, the rank-deficiency and lack of unique solution will be less important as the size of the original system matrix grows larger. Tikhonov regularizations can be considered as a version of TSVD when the system matrix is replaced by G^* in equation 3.35. To study this

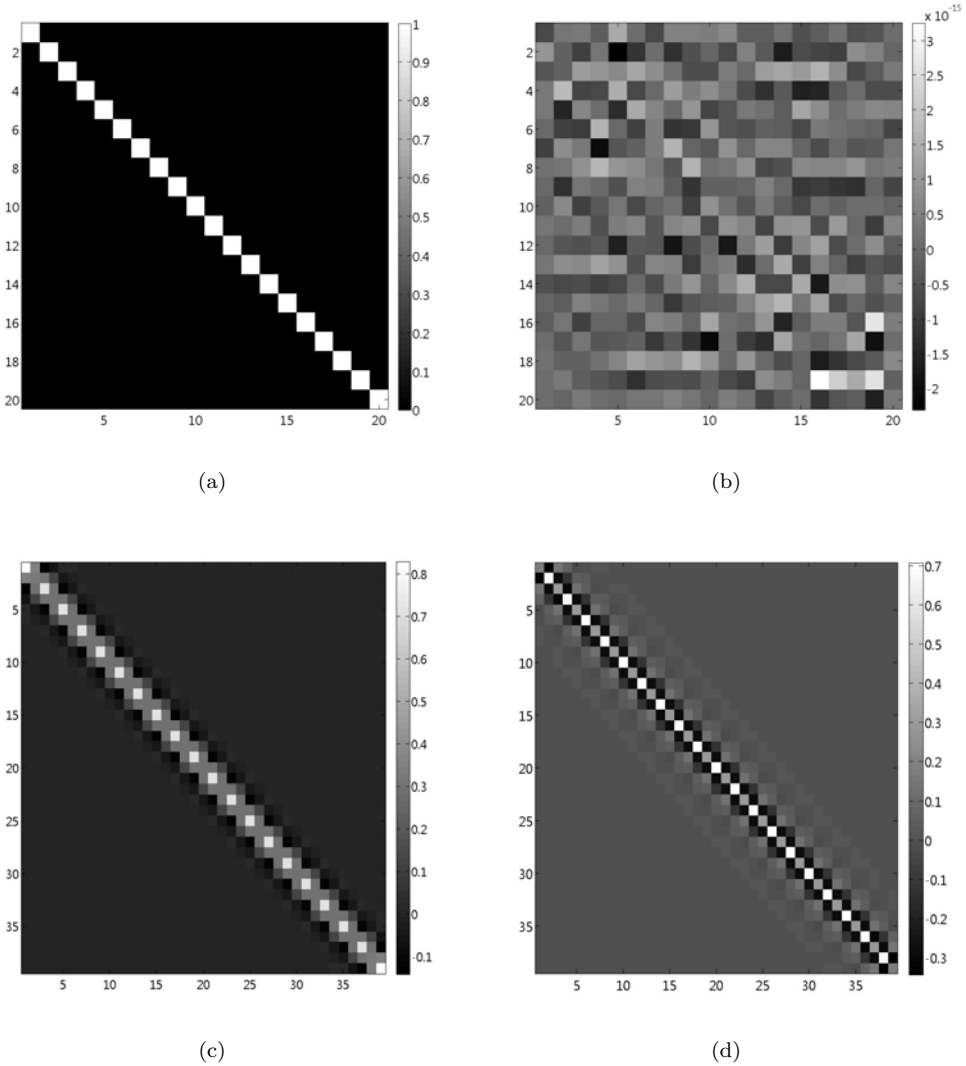

(a) (b)

(c) (d)

Figure 3.9: resolution matrices and their deviation from the unitary matrix. (a) resolution matrix and (b) deviation of the original system matrix. (c) resolution matrix and (d) deviation of the interpolated system matrix.

problem in the generalized Tikhonov regularization, we repeated the same process and calculated the singular values and the resolution matrices for:

$$R_m = G^{*\#}G^* \ \ when \ G^* = \begin{bmatrix} L \\ G \end{bmatrix} \tag{3.35}$$

The ratio of the largest to smallest singular values was found to be around 5 which shows a great stability which considering that the regularization has already been applied to the system matrix, is not surprising. The important feature is that the interpolated matrix is a full rank matrix with no absolute zero singular value.

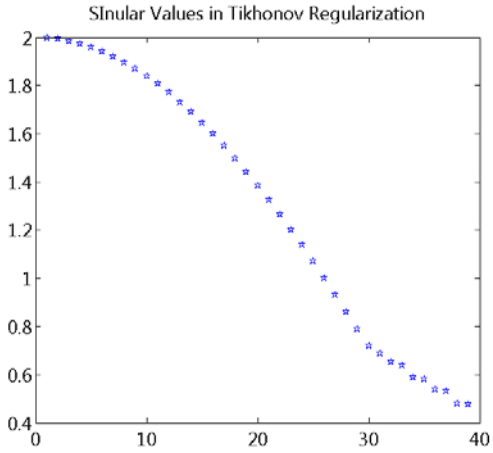

Figure 3.10: Singular values in a regularized system matrix using Tikhonov regularization. The calculated resolution matrix, also, shows a full rank resolution, very closes to the unitary matrix.

The increase in the resolution, when Tikhonov regularization is applied, vs. lack of change in the resolution when TSVD is used, explains the considerable improvement in Generalized Tikhonov vs. no significant change in TSVD.

3.5.5 Delay Correction

Delay is another source of error in flow measurement. Although perfusion model is a convolution equation and the is supposed to be time invariant:

$$\hat{c} = f.D \times G \times r = f.G \times \hat{D} \times r = f.G \times \hat{r} \tag{3.36}$$

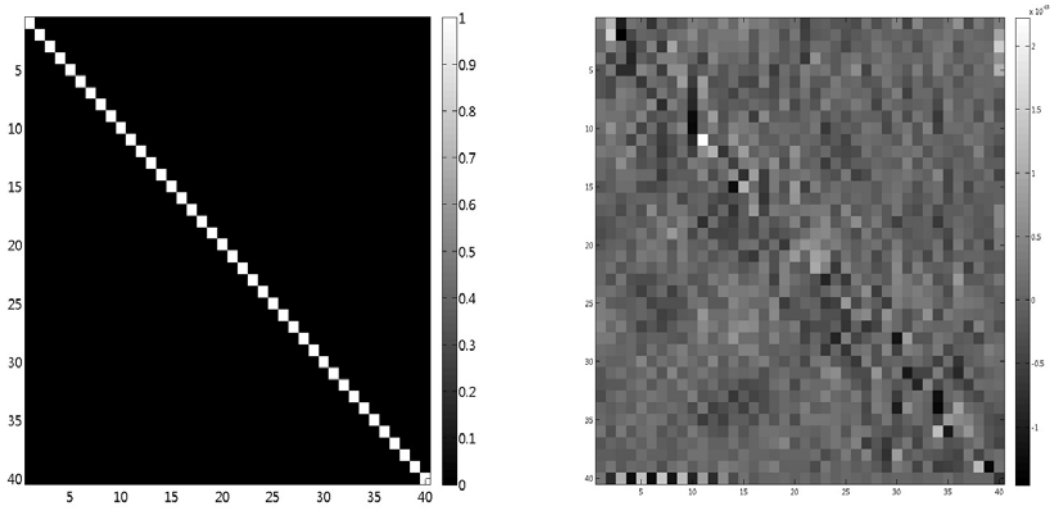

(a) (b)

Figure 3.11: Underestimation reduction using interpolation. (Left) SNR = 10 (right) SNR = 30.

delay is still considered a major problem that results in flow underestimation. In the presence of noise, regularization is inevitable. Regularization acts as a low-pass filter on the model and to fully reconstruct a delayed residue function, high frequency terms are required. Sharp edges of the initial part of the residue functions are usually smoothen by regularization which results in flow underestimation. TSVD as

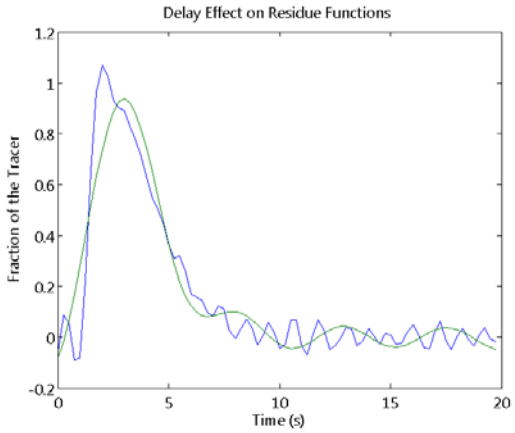

Figure 3.12: delay effect on the residue function. Applying regularization causes over smoothening and as a result flow underestimation.

well as generalized and regular Tikhonov were applied to a simulated delayed bolus

tissue signal and the flow estimation was studied. Regular Tikhonov estimated the flow rate accurately when the other two methods underestimated that. This underestimation was considerably larger in generalized Tikhonov. Large error bars in the results corresponding to this regularization method indicated that the delayed residue functions cannot be fitted into the gamma based residue model satisfactory which in turn introduced a large error to the regularization. The underestimation

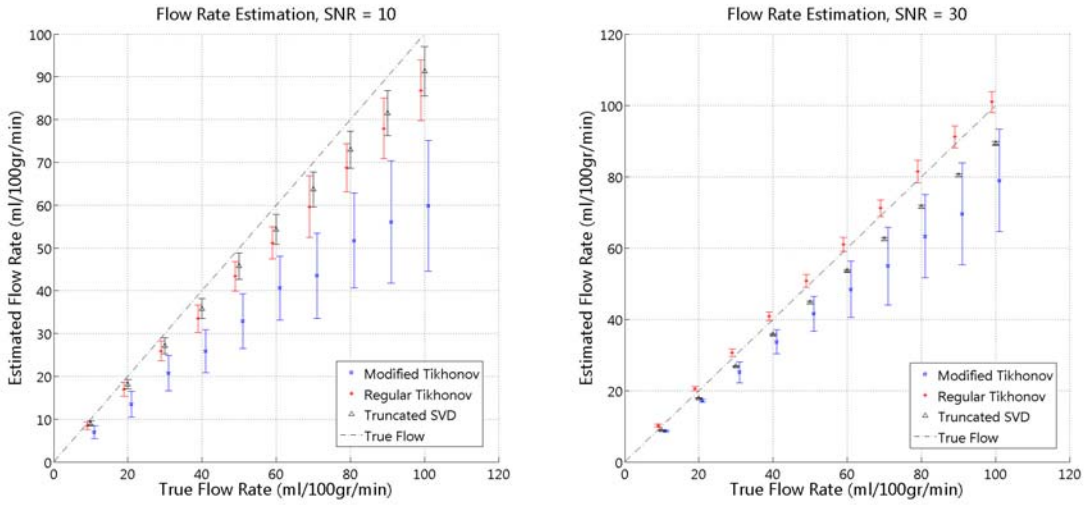

(a) (b)

Figure 3.13: Generalized Tikhonov considerably underestimates the flow rate in the presence of bolus dely SNR = (a) 10 (b) 30.

in flow estimation in the delayed bolus is also a function of the signal to noise ratio. In low SNRs it could be up to 40%. To correct the results two different approaches were applied. The first method was similar to Ibaraki approach and a new parameter, delay time, was added to the gamma based model [**?**]. Our MATLAB code was designed to discard the part of the residue function which was before the peak and fits the rest to the gamma based residue function. Again, the statistical nature of the tissue residue function is not a critical parameter here. We found that this method can be used regardless of the distribution in the true model as long as it is not very

different from the model. Figure 3.12 shows that the residue function calculated by delay-corrected generalized Tikhonov vs. residue functions calculated by the other regularizations. At low SNRs, it calculated the flow rate even more accurate than the other two regularization methods. To study the effect of systematic noise on

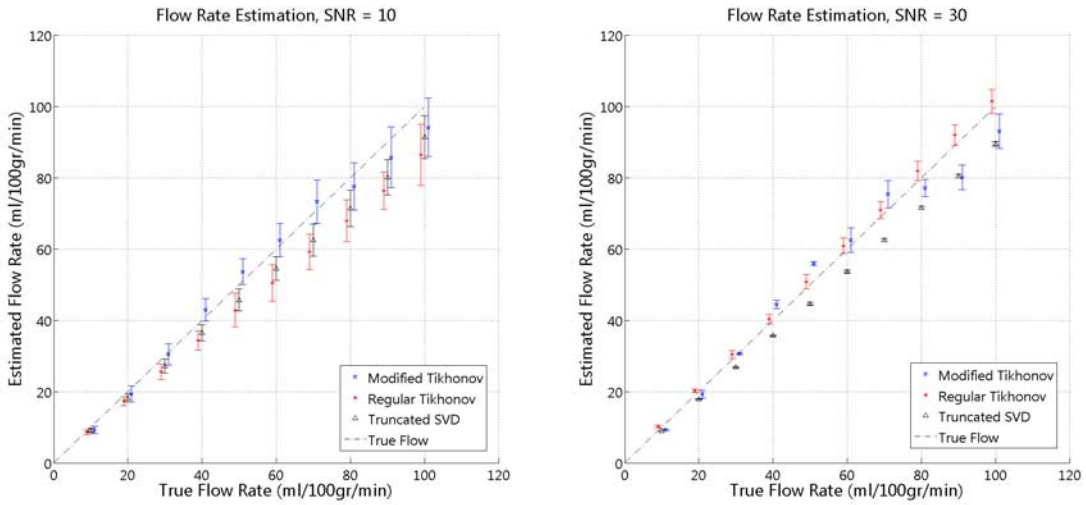

(a) (b)

Figure 3.14: Delay-corrected generalized Tikhonov vs. TSVD and regular Tikhonov at SNR = (a) 10 and (b) 30.

the calculations, data was simulated at the half of the temporal resolution of the previous simulation (TR = 2s). Simulation results show that as the temporal resolution decreases, similar delays give rise to lager underestimations. Using corrected generalized Tikhonov, flow rates were restored to the correct values, however, the error bars stayed large which was because the fitting of the delayed residue function to the model was far from ideal, due to the distortion caused by the delay to the regularized solutions.

Interpolation was tried to improve the temporal resolution. Just only interpolation (and no correction), generalized Tikhonov showed 15% improvement. The corrected regularization again showed more promising than the other two methods and recov-

ered the flow rate. However, the error bars are still larger than those in the other methods. In the second approach we estimate the delay using a lower-triangular

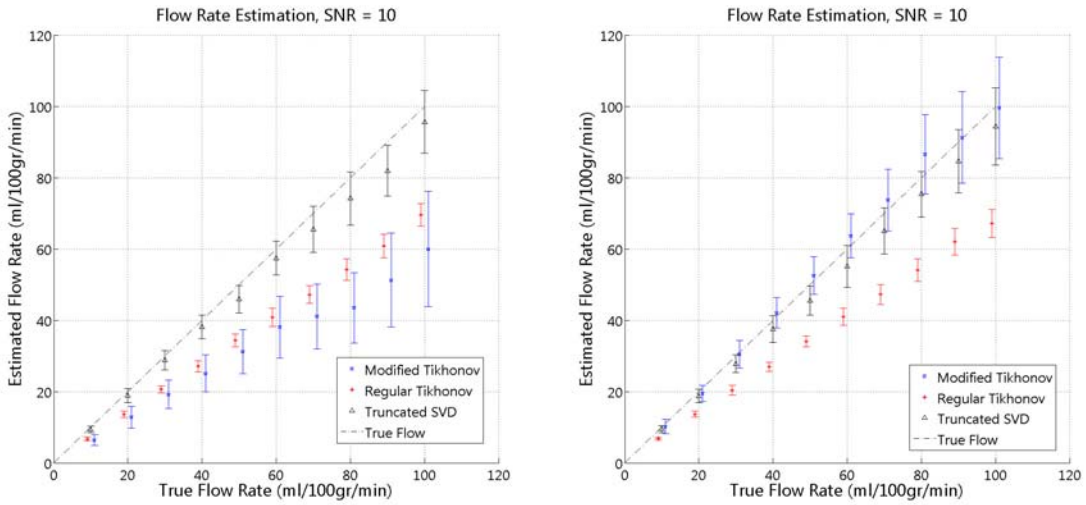

(a) (b)

Figure 3.15: (a) Both Tikhonov based regularization showed sensitive to low temporal resolution, however. (b) Generalized Tikhonov improved using delay corrected method.

matrix:

$$D = \begin{bmatrix} a_0 & 0 & 0 & \dots & 0 & 0 \\ a_1 & a_0 & 0 & \dots & 0 & 0 \\ a_2 & a_1 & a_0 & \dots & 0 & 0 \\ a_3 & a_2 & a_1 & \dots & 0 & 0 \\ \vdots & \vdots & \vdots & \ddots & a_1 & 0 \\ a_{m-1} & a_{m-2} & a_{m-3} & \dots & a_1 & a_0 \end{bmatrix} \tag{3.37}$$

The delay estimation will be an approximate method because only a limited number of the off diagonal parameters are used to minimize the computational time. If the delay is an integer multiple of the sampling time (time interval between images), the delay matrix will be in the form of a diagonal matrix with kth diagonal elements equal to one and the rest equal to zero. If the time gap is not an integer multiplication the matrix will be a multi-diagonal and the time shift will be applied through

this weighted-elements matrix. Equation 3.36 implies that the correct delay matrix minimizes the following equation:

$$\| \hat{c} - f.D \times G \times r \|_2^2 \tag{3.38}$$

The initial residue function for this process was estimated by fitting the residue function calculated from the TSVD, without any delay treatment. The elements of the delay matrix were estimated minimizing:

$$\| \hat{c} - f.D \times G \times r_0 \|_2^2 \quad \rightarrow D_0 \tag{3.39}$$

Using the calculated $\bar{r}$, and delay matrix, D_0, time shifted residue function was estimated.

$$\| c - f.D_0 \times G \times r \|^2 + \alpha^2 \| L \times D_0 \times (r - \bar{r}) \|_2^2 \quad \rightarrow r_1 \tag{3.40}$$

Figure 3.14 shows the corrected residue function for four different types of residue functions in a 2 second delay. Results show that even when a gamma based function is used for the fitting and delay estimation of non-gamma based residue functions, residue function restoration and flow estimation are accurate.

Similar to the previous approach, this method is also sensitive to the temporal resolution. Unfortunately, in this approach, interpolation did not correct the issue and caused a severe instability in the solutions.

3.5.6 Dispersion

The dispersion effect on residue functions was modeled by convolving a Gaussian density distribution to the previous model. Since the regular Tikhonov is not sensitive to the dispersion the generalized Tikhonov also is expected to not to be sensitive unless the model is a far estimation of the true residue function. The nonlinear optimization code in MATLAB estimated the parameters of the Gaussian distribution

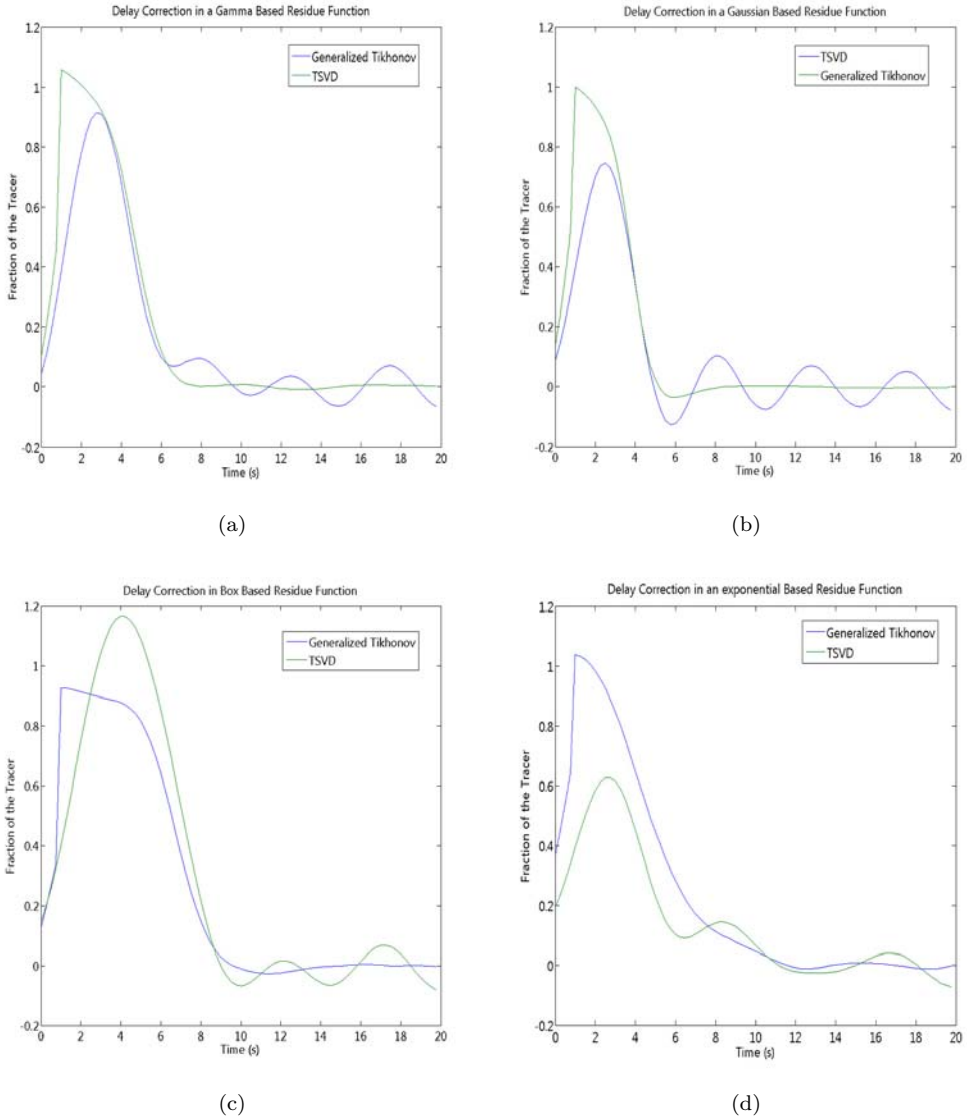

Figure 3.16: second delay correction in four different types of residue functions. (a) Gamma (b) Gaussian (c) Box and (d) exponential based residue functions.

very accurately, however, increasing in the number of the parameters that should be estimated through the optimization, moves the problem from a convex problem with a global minimum to a problem with many relative minima. In that case the gradient based optimizations will not give the correct parameters and methods such as simulated annealing should be used to find the global minima. We tried simulated annealing to find the global minima in an 11 dimensional space. The method is computationally very expensive. In the cases with limited minima, the problem can be avoided by choosing the initial parameters close to the global minimum, however, that requires some a priori information about the space that might not be available always.

3.6 Conclusion

Truncated singular value decomposition, regular Tikhonov and generalized Tikhonov were compared over different sources of error such as limited temporal resolution, thermal noise in the system, delay and dispersion. Previously, Calamante, Godian and Connelly had used regular Tikhonov to estimated cerebral blood flow. Tikhonov is a powerful regularization which has the capability of removing the oscillation from residue functions, better that any other regularization method. Unfortunately, few shortcomings such as more underestimation comparing to TSVD which has root in a misassumption in its filter has prevented a wide use of that when TSVD, in spite of the deficiency in oscillation removal and sensitivity, is still the gold standard and most popular method of regularization in MR perfusion measurement. Our goal was to improve the weaknesses of this method to hopefully see a wider used of that in future. Assuming the tracer traveling in capillaries network is a Poisson process

we defined an expected residue vector and used that to reduce the fluctuations not by reducing the change in the slop of the curve, uniformly everywhere, but by removing the oscillations around the expected residue vector. We called this method generalized Tikhonov. The other advantage of this method is to open a window to introduce priori information to the Tikhonov regularization. MATLAB simulations showed that generalized Tikhonov can estimate flow rate as accurate as TSVD. The problem with over flattening the residue function is completely resolved and it does the oscillation removal job even better than regular Tikhonov. In spite of preservation of the slop of the residue functions, generalized Tikhonov is as sensitive as other methods to short mean transition times. Interpolation was used to improve the temporal resolution and short mean transition times. Row interpolation pushed the system matrix in TSVD toward rank-deficiency and made the matrix more vulnerable to instability. In Tikhono regularization, the Tikhonov matrix saves the system matrix from rank-deficiency problem. Resolution can be improved by interpolation without the fear of the vulnerability to instability. The only problem was that the l-curve criterion does not return the optimum regularization value when the number of the columns of the system matrix is close or larger than the number of rows. In such cases l-curve overestimates the regularization parameter and causes a large underestimation in flow rate. The problem is not as severe as regular Tikhonov in the generalized method. Although this puts a limit on the temporal resolution that can be achieved by interpolation, still Tikhonov receives a considerable benefit from interpolation. The regularization parameter in equation 3.29 and the parameters of the gamma-based residue function in equation 3.31 are estimated through optimization methods. To optimize the regularization parameter, α, two methods, L-curve and 'generalized cross validation' were examined. L-curve showed acceptable in the mod-

erate to high noise regimes. However, at high signal to noise ratios no clear corner existed. Generalized cross validation in the white noise dominant simulation showed more promising, however, in actual experiment and in the presence of systematic error it would be different, as we will talk about it in more details in the next chapter. As mentioned before, the expected value for the residue function is calculated using a gamma distribution based residue function. Gamma parameters were estimated using curve fitting. Several optimization methods were used to estimate the parameters. At the beginning simulated annealing was used to estimate the parameters, since the problem is not a convex optimization problem. Simulated annealing has the advantage of the capability of finding the global minimum in the presence of many close relative minima. In all of our simulations, simulated annealing found the global minima very accurately. The only problem with this approach was that it is slow. A more careful study showed that the number of minima is limited and by defining a region of trust and choosing the initial values of optimization in this region, the problem can be reduced to a quasi-convex problem and solved with fast gradient-based methods. The three regularization methods were examined for delay sensitivity. TSVD is sensitive to delay and this sensitivity becomes more significant at low temporal resolutions. Regular Tikhonov showed not sensitive to delay, maybe because flow estimation at the presence of delay requires high frequency terms and quite opposite to TSVD, Tikhonov reconstruct these terms to some extent. Generalized Tikhonov showed very weak at the presence of delay unless the model is corrected. This has roots in poor model fitting since in our original model delay was not considered. Two methods were used to improve this flaw. The first method was adopted from Ibaraki approach. It improved the results but especially in low temporal resolutions it didn't show very satisfactory. The second method, which

is suggested by our group, uses a lower-triangular matrix with limited parameters. This method showed very promising in delay correction.

SNR = 5	Gamma	Gaussian	Exponential
Generalized Tikhonov	91.3± 2.0	94.3± 2.3	83.0± 3.2
Regular Tikhonov	83.9± 1.0	90.8± 2.0	65.9± 1.0
TSVD	95.6± 2.4	99.7± 2.5	83.6± 2.5

SNR = 10	Gamma	Gaussian	Exponential
Generalized Tikhonov	89.5± 0.8	91.6± 2.3	80.6± 1.0
Regular Tikhonov	87.3± 1.3	92.7± 2.2	70.7± 0.7
TSVD	91.0± 1.1	96.7 ± 2.5	80.0± 0.8

SNR = 30	Gamma	Gaussian	Exponential
Generalized Tikhonov	88.1± 0.2	91.7± 0.2	79.9± 0.2
Regular Tikhonov	92.0± 0.5	103 ± 0.5	77.1± 0.3
TSVD	90.1± 0.1	96.6± 0.1	77.9± 0.1

SNR = 100	Gamma	Gaussian	Exponential
Generalized Tikhonov	88.3± 0.1	92.8± 0.1	79.6± 0.1
Regular Tikhonov	88.1± 0.1	103.9±0.1	77.1± 0.1
TSVD	90.1± 0.1	96.5 ±0.1	77.7± 0.1

Table 3.1: Flow estimated in SNR = 5, 10, 30 and 100 using three different residue functions. Each value in the table represents the average of 50 simulations.

CHAPTER IV

EXPERIMENTS AND ANALYSIS

In the previous chapter we proposed a new approach to improve flow estimation using generalized Tikhonov regularization. Also we suggested some other improvements in regard to regularization parameters estimation and the delay sensitivity reduction. The mathematical simulations were used to support the theoretical calculations. To investigate the accuracy of the flow estimation in actual experiments we have designed a microfluidic perfusion phantom which in terms of many vascular parameters is similar to actual tissues. Many of the flow dynamic and imaging features such as hemodynamic behavior, tracer diffusion and signal to noise ratio are functions of the size of the capillaries and the vasculature, previously used tubing phantoms cannot be considered as a reasonable tissues phantom in experiments. We believe our microfluidic phantom provides a more accurate medium for perfusion simulation comparing to such phantoms.The other advantage of using this microfluidic phantom is that the experimental condition will be fully reproducible. We used microfabrication lithography technique to producea pattern of microchannels in the similar range of tissue capillaries. This simple and inexpensive technique gave us the capability of making new phantoms in only few hours. A variety of vascular architectures and a wide range of vascular diseases can be simulated with these phantoms.

Delay and dispersion as two major sources of error in flow estimation can be added and fully determined in these samples. In the following chapter, using COMSOL, a finite element method software, we calculate the flow everywhere in our phantom and use that information to verify the accuracy of our mathematical approach.

4.1 Perfusion Phantom Design

Microvasculature morphology, especially in the brain tissue, has been studied by many groups. The topography of microvasculature of cortex, topology of coronary capillaries, the architecture of cortical and subcortical capillary network in brain and also the microvasculature architecture in pre-cancer and tumors [32, 47, 39, 36] are among these studies. Blood supply in brain tissue, microvasculature structure as an indicator of tumor treatment effectiveness and the modeling of revascularization are few of the motivations of these studies. To design a capillary network for our perfusion phantom we relied on Murray's "minimum work" model. Murray's model is based on the nature preference for minimum energy loss in the vascular tree assumption. The loss in energy is defined as the sum of kinetic energy consumption given by the product of flow and pressure drop and chemical blood maintenance energy which is proportional to the blood volume. To satisfy the minimum work principle in the [micro]-vascular, the diameter and the branching angles should follow these relations:

$$\frac{r_0^3}{f_0} = \frac{r_1^3}{f_1} = \frac{r_2^3}{f_2} = constant$$
$$Cos(\theta_1) = \frac{r_0^4 + r_1^4 - r_2^4}{2r_1^2 r_2^2},\ Cos(\theta_2) = \frac{r_0^4 + r_2^4 - r_1^4}{2r_1^2 r_2^2} \tag{4.1}$$

A phantom, designed based on Murray's law, was independently proposed by our

group and Emerson et al. Emerson [16] and his colleges used their "biomimetic microfluidic manifold" to study Murray's law on microvasculature bifurcation. Now that we have a model that discribes the branching, we need to determine other parameters of the network including the diameter of the parent vessel and the following generations of the capillaries, the bifurcation point or the capillaries' segmental length and the distance of the parallel capillaries. Kassab and Fung have done a research on topology and dimensions of pig coronary capillary network and have provided the average and the distribution of these parameters for different generations[32]. The first generation of the phantoms was designed with different number of capillary generations to simulate different flow transition times. We adopted the diameters, the segmental length and the distance of the capillaries for the smallest part of the network from the literature. Then based on the Murray's law we generated the previous generations to the parent channels. The parameters were calculated directly from the Murray's law. The round cross-secrions were translated to rectangular cross-sections since the micro-channels have rectangular cross-sections. In the second generation

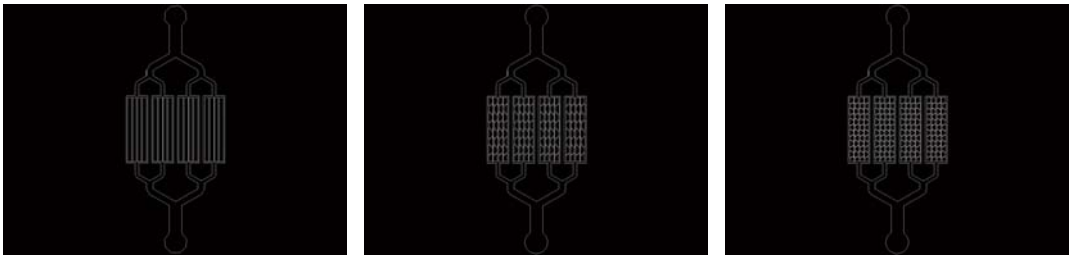

(a) (b) (c)

Figure 4.1: First generation of the phantoms. (a) short (b) medium and (c) long transition time phantoms.

of the phantoms modified equations were used. These equations apply Murray's law to constant-depth channels with rectangular cross-sections:

$$\alpha_n(1+\alpha_n)PO(\alpha_n^*) = (2X)^n\alpha_0(1+\alpha_0)PO(\alpha_0^*) \tag{4.2}$$

Where X is the branching parameter, PO is the Poiseuille number. The important note here is that the $\alpha_n^* = \alpha_n = d/w_n$ when depth, d, is smaller than width of the channel, w_n, or $\alpha_n \leq 1$. If the width is smaller than the depth of the channel then $\alpha_n^* = w_n/d$, however, α_n remains the same. The average diameter, segmental length before branching points and distance between two adjacent capillaries for the fifth generation were chosen 25µm, 50µm and 100µm, respectively. Of course, a more realistic phantom needs more capillary generations with diameters down to few microns.

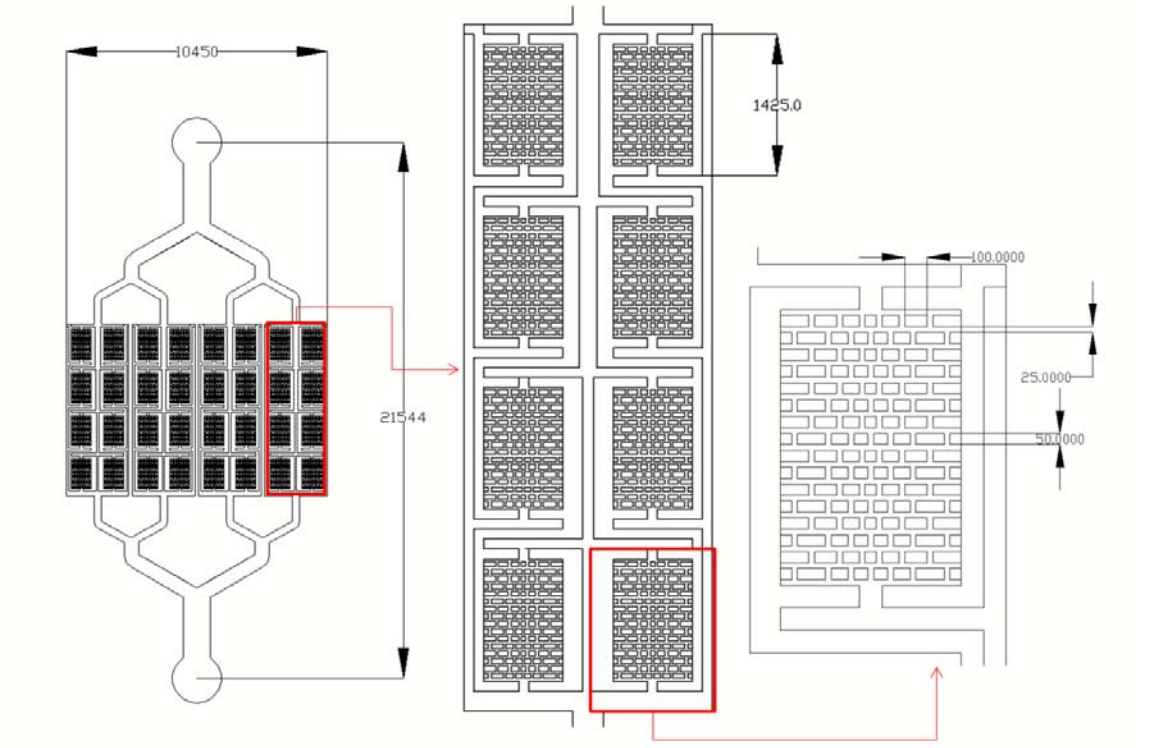

Figure 4.2: The second generation of the perfusion phantom with corrected dimensions.

4.2 Lithography Microfabrication

Using Microfabrication lithography technique, micro-channels with few microns to few centimeters in width, few to few hundreds of microns in depth and networks with

any desired pattern can be generated. In last two decades, this powerful technique has had a significant impact in integrated circuits design and now is widely used in designing microfluidic devices. Taking advantage of this method, we have been able to create a perfusion phantom which is very similar to actual tissues in terms of capillaries scale and density. In this process a silicon wafer is coated with a photo-resist material. Then the wafer is baked to cure the photo-resist. In the next step coated wafer is exposed by UV light. The mask will be placed between the UV lamp and the wafer. In the presence of the reactant material, and when exposed to UV wavelength, small molecules of the photo-resist bound together and create heavy polymers. This process is referred to as cross-link. Then the wafer is immersed in development solution which removes the unexposed SU-8. Last step would be a hard bake to increase the strength of the photo-resist.

4.2.1 Mask Preparation

The first step in microfabrication is to design a lithography mask. This mask will be used to transfer the desired patter to photo-resist material during UV exposure process. Transparency masks and chromium masks are two types of the masks we used in our design. To make transparency masks, the desired pattern is printed (CAD/ART Incorporation) on regular transparencies. The highest possible resolution in this type of mask is limited to 10m which requires 20000 DPI printers. In practice even this resolution might not be possible to be achieved. Transparencies are not perfectly transparent at UV wavelength. Also, the black ink is not fully opaque at this wavelength. The other problem is that most of the UV exposure systems are designed for glass masks. Due to the difference in refraction index in air and transparency, any air gap between the wafer and the flexible transparency mask at the contact surface causes UV diffraction. Consequently, the features in the

pattern will not have perfect edges. When the features are very close and the aspect ratios of features are high features diffuse into each other. However, based on our experiences, it is a good and inexpensive solution for patterns that have aspect ratios of 4 or smaller and when the highest resolution in the pattern is 25µm or higher. We used this type of mask in the first generation of our phantoms.

The second type of masks, a glass slab coated with chromium photo-resist, is more expensive to create. However, using chromium masks even submicron resolution can be achieved. To make this type of masks, the pattern designed in AutoCAD, saved in DXF format, was translated to GDF format using L-edit software. This software fractures the pattern to rectangles since the mask maker uses rectangular flashes to draw the pattern on the mask. To decrease the process time curves should be avoided, as much as possible. Our design was fractured to 18000 flashes. The process took 5 hours. The flash rate was 3600 flash/h (1 Hz). Then the mask was immersed in the developing solution for few minutes. In the last step, the mask was first rinsed with acetone and then with DI water and evetually dried with air.

4.2.2 Photo-resist Coating

SU-8 2100 (micro chem. Corp.) was used as the photo-resist. SU-8 is a negative photo-resist. SU-8 2100 has very high viscosity and it make it difficult to work with, however, since we needed thick layers, ¡ 200m, the only options were SU-8 2100 and 2150, which both have very high viscosity. To spin coat, 4-6 cc of SU-8 2100 was poured on the wafer which was centered on the spinner. The spinner was set to 60 seconds of spreading at 500 rpm and 100 rpm/s acceleration and then 30-60 seconds of spin at 1250 rpm with 250 rpm/s. Then the edge beads were removed with EBR PG solution (micro chem. Corp.) when wafer was spinning at 500 rpm for 30 seconds. Edge beads removal is very important, especially in coating with viscous

SU-8s. The thickness of the beads was measured up to 3 times of the thickness in the center. Such thick beads in the peripheral area of the wafer prevent good contact of the mask and the wafer in the UV exposure process. Then the wafer was baked

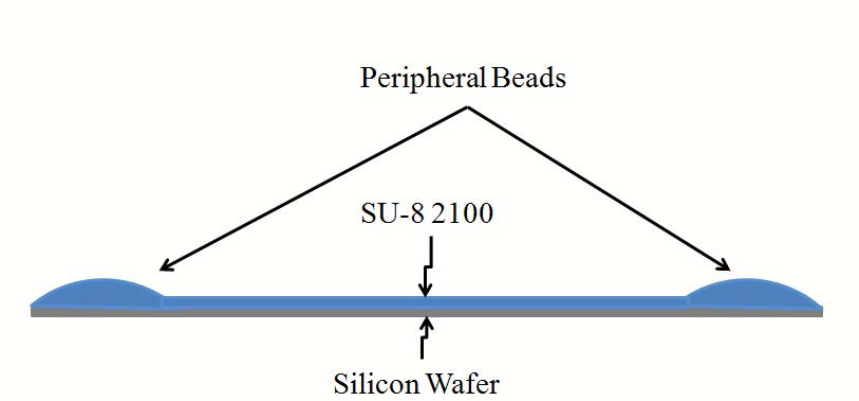

Figure 4.3: Peripheral bead in SU-8 coating prevent the full contact of the mask and the wafer in the exposure procedure.

on the hot plate at 65℃for 7 minutes followed by another 2 hours of baking at 95℃. Then the hot plate was turned off and the wafer was left on the plate for an hour to cool down to the room temperature. The cooling step is very important because the SU-8 on the hot wafer will not cure no matter how long it is baked and at the UV exposure step the wafer will stick to the mask.

4.2.3 UV Expose

As mentioned before to complete the cross-link process photo-resist needs to be exposed by UV wavelength. The exposure time is a critical parameter in the micro-fabrication process. If the sample is under-exposed the cross-link will not complete and the features will not cure and will be washed out in the development process. Also, it is possible that the surface cures when the cross-link has not completed deep in the coating which results in wedged features that are thicker in top. Such features are usually very fragile. Using MA/BA-6 Mask/Bond Aligner, a set of different

exposure time/energies, from 1650 to 4800 mJ/sq.cm at 365 nm (i-line) was tried. The best result was achieved at 4200 mJ/sq cm. We found over-exposing much less harmful than under-exposing. That is generally true about all negative photo-resists. The system supports a wide range of contacts including soft, hard and vacuum. In soft contact the wafer and the mask are brought to soft contact. In hard contact a slight pressure is applied and in vacuum mode a vacuum is applied to prevent air gaps. These features are very important in high aspect ratios exposure. We used hard contact due to high aspect ratio of our features (¡10). Also, we found coarse-test wafers are not perfectly flat which causes non-uniform exposure along the wafer. When the wafers were replaced by primer wafers the problem was resolved.

4.2.4 Development

After UV exposure the wafer was baked again at 95C for two hours and then the wafer was cooled down to the room temperature on the turned off hot plate for an hour. Then Micro chem. Corp. development solution was used to develop the wafer. As mentioned before, in this process the blocked photo-resist is washed out. We left the wafer in the development solution for 17 minutes, however, that could be very different from wafer to wafer. During this time the solution should be stirred to bring the fresh solution into contact with the wafer. Then it was rinsed with fresh SU-8 development solution for 10 seconds followed by a rinse with Isopropyl alcohol for 10 minutes. Then the wafer was dried with air. At this level features can be checked under microscope for the sufficiency of the development. Development is usually followed by at least two hours of hard baking at 95C for improving the strength of the SU-8. Figure shows the developed wafer.

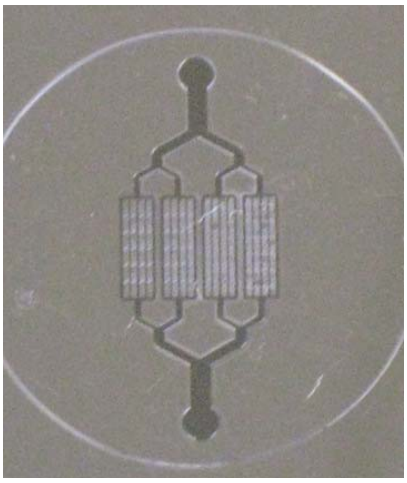

Figure 4.4: A developed wafer coated with SU-8.

4.2.5 PDMS Curing

Polydimethylsiloxane (PDMS) is a silicon based polymer which is widely used for microfluidic devices. PDMS (Dow Corning Co.) is a two component material, Polydimethylsiloxane and the curing agent, which should be mixed in the ratio of 1:10. The mix is rather viscous. During the mixing the two components air bubble usually get trapped and if PDMS cures before bubbles are removed they might ruin the device. The mix should be degassed in a vacuumed chamber for at least 20 minutes or until bubbles are completely gone. Then the PDMS is poured on the top of the mold and is placed in the oven. We found it helpful to degas the PDMS after pouring the solution on top of the mold as well. Oven was set to 65C and the sample was baked for at least 3 hours.

PDMS bounds to wafer very strongly through a silicon bonding. That prevents peeling the PDMS from the mold. To overcome this problem, mold should be coated with Silane. For that purpose, hard-baked mold is placed in an a vacuum chamber with Silane to be coated by chemical vapor deposition (CVD) method.

To measure the height of the features a PDMS sample was sacrificed. The sample

was cut along the height of the features. Using microscope, depth of the features were measured to be 270 18m, in several spot. The 6.7% deviation is because we used SU-8 at the very edge limit of its applicability. SU-8 is usually used for aspect ratios of ¡10 and in our design this ratio was around 10.8.

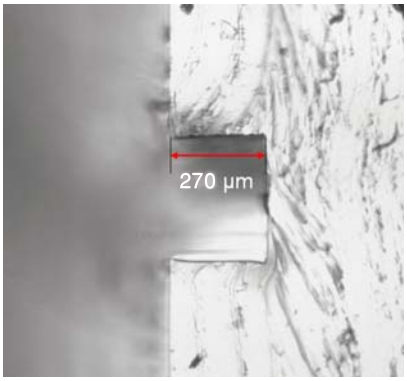

Figure 4.5: Features' height measurement using PDMS sample.

4.2.6 Plasma Oxygen Welding

To secure and close the open side of microchannels the PDMS sample needs to be welded to a glass substrate. Plasma oxygen welding is an easy method which can be done in a very short time. To prepare the sample, it was cut in 25mm x 25 mm blocks with the pattern in the center. Then 2mm reservoirs were punched for the input and output flows. Then the PDMS cutout and glass substrates were treated with corona oxygen plasma (electro-technic product inc.). This treatment increases the surface energy and causes PDMS-Silicon polymerization. Also, PDMS is a hydrophobic material. Conducting the flow through such tiny micro-channels in hydrophobic PDMS create a considerable resistance. Treating the surface with plasma oxygen, temporarily, changes this characteristic towards hydrophilicity. Dry surface keeps the hydrophilicity for about 10 minutes. This period can be prolonged by keeping the surface wet.

4.2.7 Flow Simulation

As mentioned before, the perfusion phantom generated using the above method is used to verify the accuracy of the estimated flow. Using finite element method software such as COMSOL multyphysics (formerly Femlab), the flow dynamic in every point of the sample can be calculated. Assuming water as an approximation of blood and ignoring the hematocrits effect, we used the simple navier-stokes model for the Newtonian fluids. However, the software has the capability of calculating the flow dynamic for nonlinear fluids as well.

4.2.8 Flow Calculation

As mentioned above, the steady state incompressible navier-stokes model was used for the flow calculation. The CAD design was imported by the CAD interface included in the program. In the next step the inside and the outside volume as well as the boundaries of the channels were defined. Then the grid mode was applied to create a network of triangles for the purpose of finite element calculation. Accuracy and the resolution increases by finer grids, however, it makes the problem computationally more expensive. To keep the grid resolution efficient we used the smart grid option which provides higher density in smaller features. In the next step, the physical parameters such as density, dynamic viscosity, relative permeability and the mean free path were determined. COMSOL has a library for different materials and by choosing the material/fluid it automatically sets the values. Table show some of this values.

The boundary condition at the input and output were set to the input and output flows and on the path and on the micro-channels' walls were set to "no-slip" which for viscous fluid states means that the fluid has zero velocity relative to the bound-

ary. No-slip boundary condition can be justified based on the hydrophilicity of the PDMS. The flow was calculated and the results were exported to Matlab for further analysis.

Parameter	Density	Dynamic Viscosity	Relative Permeability	Mean Free Path
Values	1 gr/ml	0.894 cP	80	10^{-4}cm

Table 4.1: state incompressible navier-stokes model parameters.

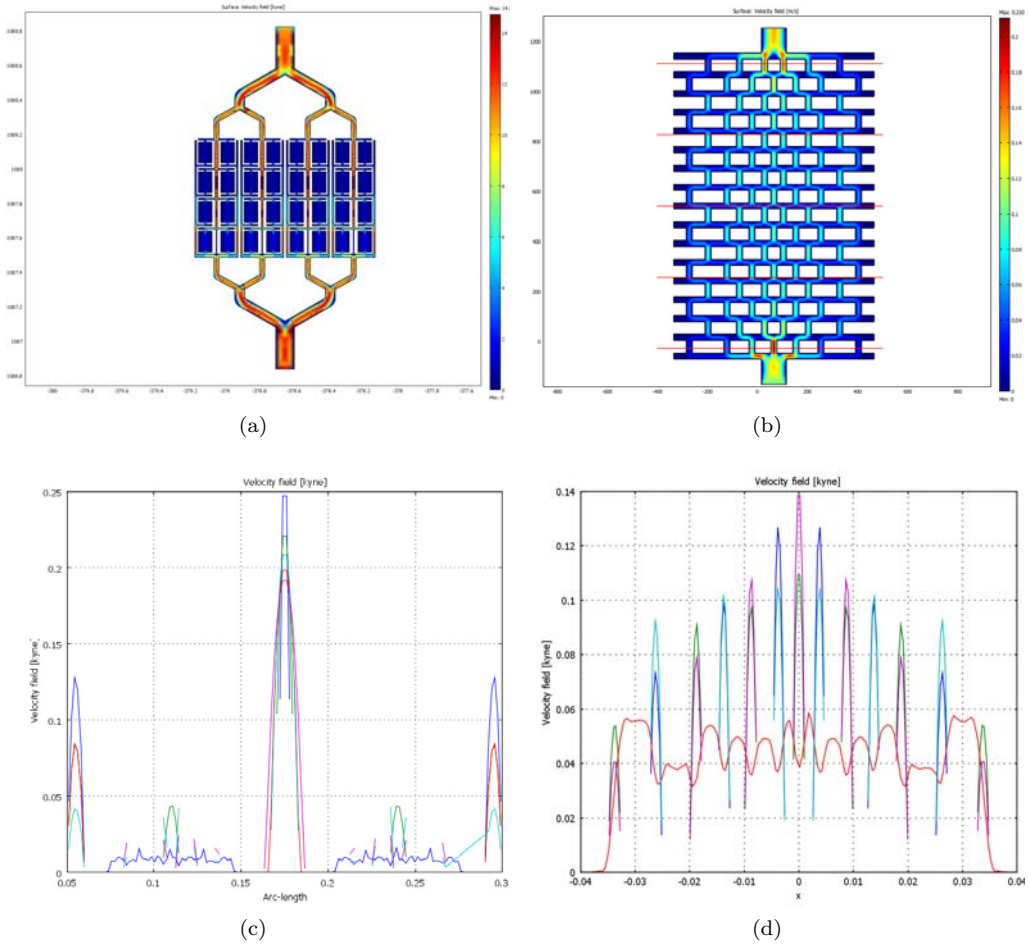

Figure 4.6: (a) the flow velocity in the perfusion phantom calculated using COMSOL, (b) high resolution magnified cell of the fifth generation micro capillaries, (c) flow at the different regions of the phantom, (d) the velocity in the different regions of the cell.

4.2.9 Residue Function Simulation

The other application of flow calculation using COMSOL is to estimate the residue function based on this information. We previously defined residue function as the instantaneous fraction of the tracer in the tissue. To calculate that using simulations we wrote a code in Matlab that chooses an infinitely small elements in the inflow and follows the flow map. Repeating this for large number of elements, h, the traveling time distribution function can be simulated/calculated. As we mentioned before residue function and this distribution are related through:

$$R(t) = 1 - \int_0^t h(\tau)d\tau \tag{4.3}$$

Figure 4.7 shows the simulation at one of the cells in the fifth generation capillaries. The central and peripheral paths give rise to the two major peaks in the graph. The output of the COMSOL is the flow velocity which is different than what we desired, the flow rate. However, using divergence theorem these two can be translated to each other. Using Matlab we wrote a code that translates the velocity to the flow rate and generates a flow map that is in the same resolution as our MR image.
For non-diffusible tracers both the substrate and the fabricated layer are made of polydimethylsiloxane (PDMS). To study diffusible tracers the substrate would be made of agarose gel since it exchanges water with micro-channels in a similar time scale as it happens in capillaries-tissues. Also our experiments show that the uptake-washout curve in agarose is very similar to that in actual tissues.

4.2.10 Plasma Oxygen Welding

Using computational fluid dynamics software, perfusion parameters including the blood volume, flow and the transition time in the micro-channels network were calculated to be in the range of brain perfusion values. The correlation between the

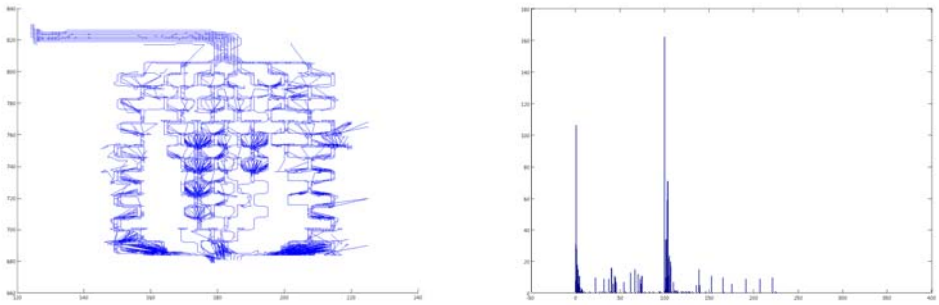

(a) (b)

Figure 4.7: (a)infinite small elements path through a single fifth generation cell (b) the traveling time distribution. The two peaks represent the two major path in the cell.

calculated and the measured values of perfusion-parameters can be used for calibration or accuracy investigation in quantitative imaging.

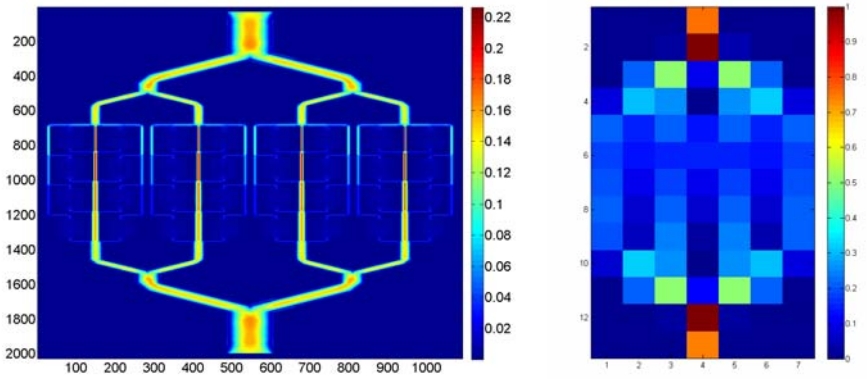

(a) (b)

Figure 4.8: (a)high resolution fluid velocity calculation using COMSOL, (left) the high resolution velocity profile was translated to flow using Matlab. Each pixel represent a MR image pixel 5/32 cm ×5/32 cm.

4.3 Experimental setup

The Microfabricated phantom was used to investigate the accuracy of the three regularization methods, TSVD, regular and generalized Tikhonov regularization[15]. The experiments were carried in a 2T NMR/MRI Varian system. Imaging was done

using a handmade surface coil. The diameter of the coil was around 5cm. The T1 and T2 of silicon were measured to be 0.64s and 9ms, respectively. For water these values are 2.45s and 2.13s.

During the imaging we noticed that the Larmor frequency of silicon is very close to the proton frequency which makes it difficult to recognize the water in the microchannels from the silicon bulk. The Silicon signal was very broad and over lapped the water signal. To remove this signal a pulse sequence was designed that would use a Gaussian RF pulse to saturate the silicon signal at the beginning of each readout. Figure 4.9 shows this pulse sequence.

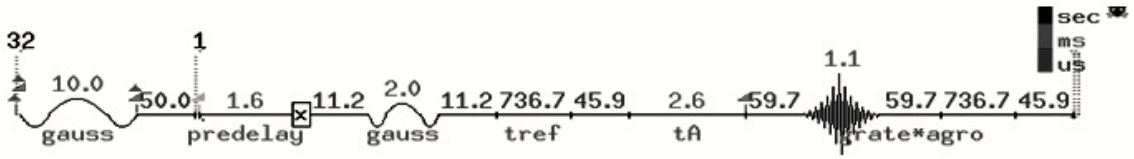

Figure 4.9: The gradient echo pulse sequence used for silicon saturation and fluid imaging.

Also, as mentioned above, silicon T2 is much shorter than that of water. This long TE of 9ms was used to remove the residual silicon signal from water FID. The TR of the sequence was 600 ms which would give us a temporal resolution in the range of actual perfusion imaging sequences. To increase the volume of the phantom several layers of microfabricated channels were installed on top of each other. That gave a three dimensional look to the phantom. The slice thickness in the imaging parameters was set to 8 mm. first a high resolution image was taken to locate the sample. As we will discuss in the following this high resolution image is critical to generate the correct flow map using the finite element method software. The actual resolution

was 32x32 pixels of an feild of view of 5x5 square cm. The resolution was around 2 square mm which is similar as the resolution of the perfusion images. Figure 4.10 shows the high and the low resolution MRI images of the phantom. Manganese was

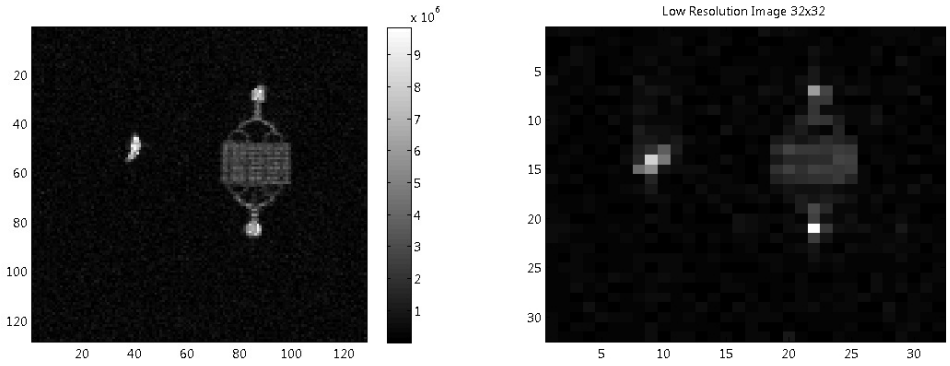

(a) (b)

Figure 4.10: (a) high and (b) low resolution images of the phantom the small bright area in the left is the tubing which was used as the artery for AIF measurements.

used as the contrast agent. To measure the relaxivvity of manganese solutions with 200Mol/L to 50mMol/L were prepared and the T2s were measured. The relaxivity was measured 84 L/(Mol s).

Figure shows the setup of the experiment. A transfusion pump was used to provide a precise flow. The system has the capability of generating flows in the range of 0.1 ml/h to 1000 ml/h. A T valve was plugged close to the phantom to inject the contrast agent. In each measurement a bolus of 300µl of the 25mMol/l manganese solution was injected. MRI images clearly show the passage of the contrast agent through the phantom.

4.4 Experiment

Several sets of data, at flows rates 6, 12, 18, 24, 30, 36, 42, 48, 54 and 60 ml/h with temporal resolution of 0.6 s were collected. Due to small TR/T,1the flip angle

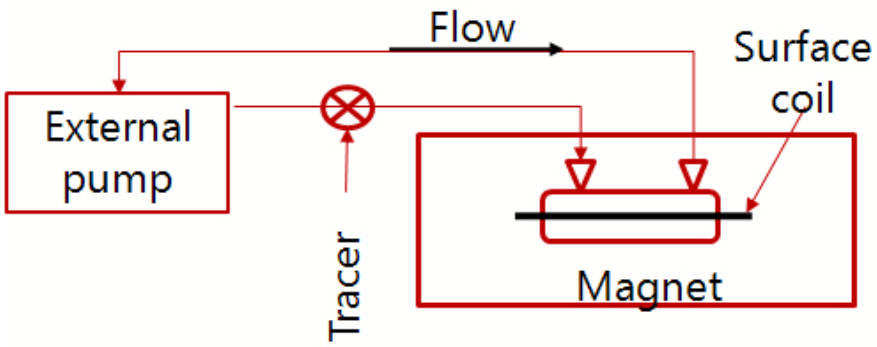

Figure 4.11: The setup. An external pump provides the flow into the sample. The tracer is injected close to the phantom for tighter bolus.

was calculated according to the Ernst equation to be between 7-10°.

4.4.1 Noise Effect

To study the effect of noise on the flow estimation the experiment was repeated 5 times for each flow rate. To separate the thermal noise from the systematic noise, all data sets were set to a similar number of data points. For example if 90 points were collected during the bolus passage at flow of 60 ml/h, the data set of flow of 6 ml/h was down-sampled at the ratio of 1 to 10. Data sets generated with this method are very similar since the regularization cannot recognize between lower and higher temporal resolution as long as the ratio of sampling and the flow is constant. In the actual experiment, since we are working in a Newtonian fluid domain, change in the flow will be linear in the phantom and proportional to the change in the input flow. The only nonlinear effect is the diffusion of the contrast agent on the way from the valve to the phantom. In low flows the bolus is broader than fast flows (figure 4.12). Due to the high noise, AIFs were fitted to gamma functions and the functions were used to generate system matrices in deconvolution process.

Three sets of data with signal to noise ratios of 18, 25 and 36 from data sets with 180 to 1800 data point were generated. The new data sets had 45 data points.

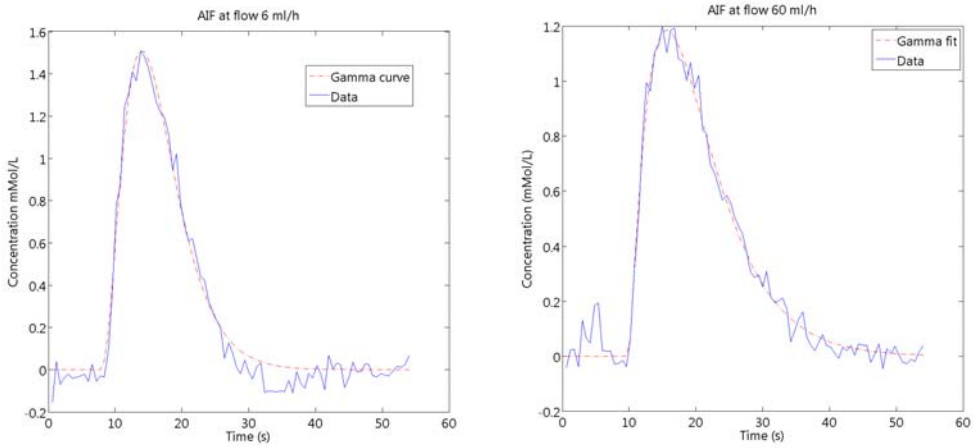

(a) (b)

Figure 4.12: AIF at two flows (a) 6 and (b) 60 ml/h. both flows are sample with 90 data points.

Each point was averaged 1 to 4 times to simulate different SNRs. Figure shows the estimated flow at the three SNRs. We didn't consider regular Tikhonov in many of our analyses because the result were very instable. The two regularization parameter criteria, GCV and L-cure were the main reason of the instability. GCV clearly underestimates the regularization parameter. This is because GCV cannot recognize the systematic error and only considers the white noise in the system [24]. The corner in the L-curve were missed and we had to add some white Gaussian noise to the data to enhance the corner. This problem happens in very high SNRs, however, this time we were experiencing it in low SNRs [29]. At all SNRs the two method underestimated the flow rate by 22%. Part of this high underestimation is due to the exponential residue function. As we mentioned in chapter III this type of residue function has the highest rate of underestimation. High temporal resolution is required to reconstruct fast decaying residue functions. Results shows that the average of the underestimation is not changing by the noise level. However, the height of the error bars does considerably change by the thermal noise.

The second group of data sets were generate with the goal of studying the tradeoff

between the systematic noise by caused low temporal resolution vs. the thermal noise. The temporal resolution in the second data set was 4 times higher than that in the previous set. Figure shows the results. Obviously the error bars are larger. However, the flow estimation was improved by 12-14% for generalized Tikhonov and TSVD, respectively.

4.4.2 Delay Correction

Flow at the two sides of the phantom was calculated. AIF was measured very close to the one side to minimize the delay when the other side would experience 2-12 seconds of delay depending on the flow rate. Both methods experience similar amounts of underestimations. Also, the results showed that the effect of the delay on the data sets with high temporal resolution is very small. At low temporal resolution and SNR (worst case scenario!) the underestimation went up to 55%. At high temporal resolution and SNR, the minimum underestimation was 22%. This implies even in the best case, delay correction is required. The flow, at the other side of the phantom, was showed to underestimate the flow by 37%. Delay was corrected using the two method mention in chapter III. The first method, fitting the curve to the model, restored the flow to 71% of the true flow. The second method, shift matrix with limited elements, corrected the flow to 83% of the correct flow rate.
SMLE is computationally expensive. As figure 4.15 shows, as the temporal resolution decreases in higher flow rates, its accuracy also decreases while the fitting based method is insensitive to the temporal resolution.

4.4.3 Temporal resolution Improvement

As mentioned before, one way to improve the temporal resolution is to interpolate the row elements of the system matrix. Increasing the resolution by 50% improved

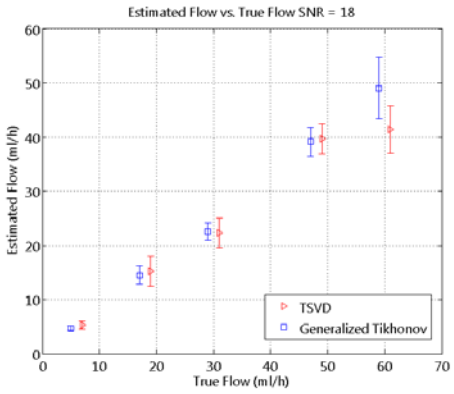

(a)

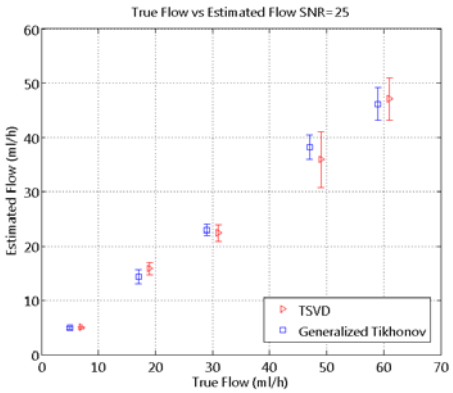

(b)

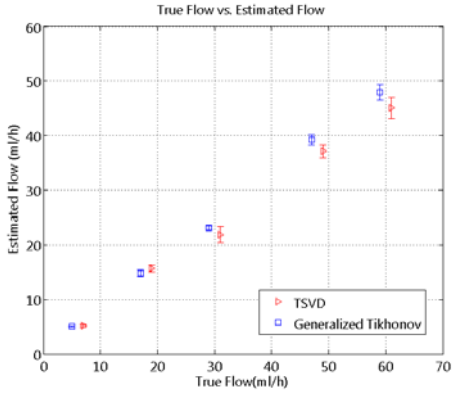

(c)

Figure 4.13: Flow estimation in different noise levels. Three data sets with signal to noise ratios 18, 25 and 36 were generated. The average of the flow is not a function of noise, however, the error in estimation is dependent on the noise level.

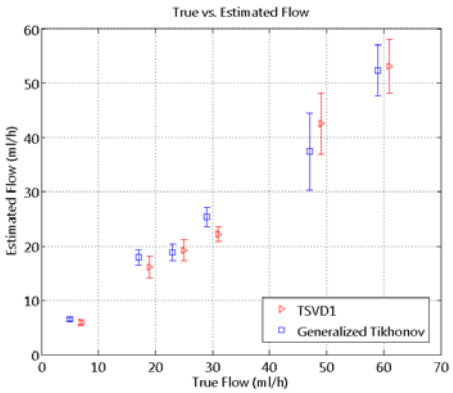

(a)

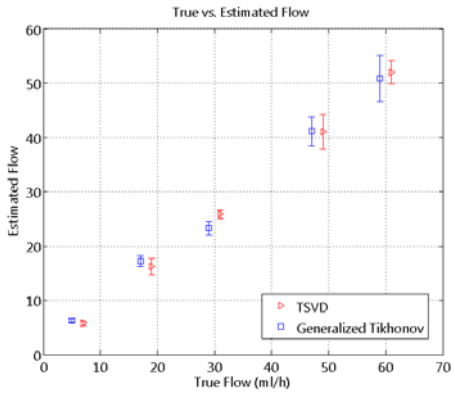

(b)

Figure 4.14: Flow estimation at low signal to noise ratio and high temporal resolution. The average of flow shows 12-14% improvement.

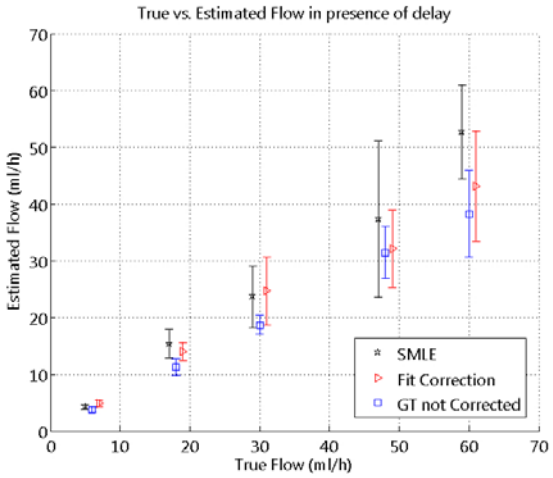

Figure 4.15: Delay correction. The delayed data was corrected using fitting method and shift matrix with limited elements. The 37% underestimation was improved to 29% and 17% for the fitting-based method and SMLE, respectively.

the flow rate accuracy by 8%. Instability issue, for resolutions higher than 50%, were clearly amplified. Figure 4.16 shows the improvement in interpolated data vs. the not interpolated data.

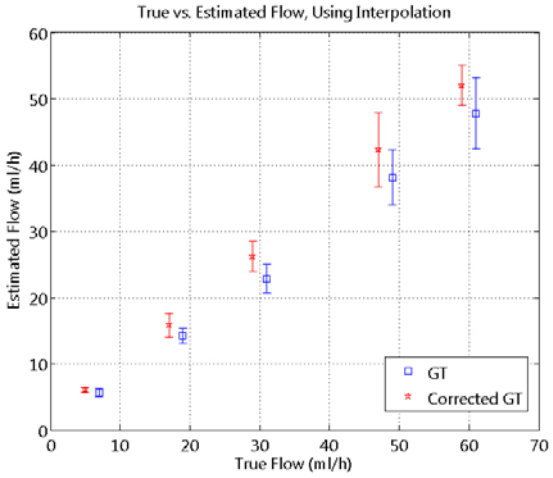

Figure 4.16: The row elements of the matrix was interpolated and the up sampled by 50%. Result showed 8% improvement over flow calculation using the original system matrix.

4.5 Conclusion

Using a microfabricated phantom, perfusion measurement in brain tissue was simulated. Perfusion-related parameters of the phantom were similar to those parameters in actual tissues. The generated data was used in studying Generalized Tikhonov and comparing that to the gold standard method, TSVD. Both methods underestimate the flow rate by similar amounts. The underestimation was mostly due to the low temporal resolution rather than thermal noise. Using interpolation, this problem can be improved in generalized Tikhonov regularization. TSVD does not show much improvement due to up-sampling and the instability appears very soon. Delay correction was also improved using fitting-based and shift matrix. Shift matrix showed more promising than the other methods, however, due to large volume of required computation, its application will be limited to the low temporal resolution matrices.

CHAPTER V

CONCLUSION

This research started with the aim of using laser polarized xenon as a tracer in perfusion measurements. Xenon due to its non-toxicity, high diffusibility into tissues and the capability of polarization enhancement was assumed to be a very promising candidate for cerebral blood flow measurement. Since there is no natural xenon in tissues, no background signal subtraction is required. Also, some other errors caused by background tissue signal such as partial volume error in arterial input function measurement can be avoided. This gives rise to the possibility of local AIF measurement in smaller arteries which results in bolus delay and dispersion error reduction. However, some disadvantages with this method convinced us that it might not become a routine clinical method for CBF measurements. Maybe the most important problem is that xenon is an anesthetic gas and considerable and sudden blood flow reductions as result of being exposed to xenon have been reported in the scientific literature[7]. The other shortcoming is that the enhanced polarization is not reproducible in the body. Fast relaxation in the blood and rapid decay due to the RF pulses destroys the polarization in a very high rate. One suggestion to overcome this problem was continuous delivery of xenon dissolved in a solvent. The xenon needed for such methods was estimated using simulations. Two objections to this

method are 1) for CBF measurements high temporal resolution is required and the xenon delivery is limited by the blood flow and the xenon solubility in blood. Even using carriers such as PFOB might not provide enough xenon in a short time. 2) high dosage of xenon causes blood flow reduction in response to this anesthetic gas. 3) In addition to all these problems, xenon T_2^* in blood is very short, around 20 ms, which makes the current fast spin imaging techniques such as EPI inefficient. Other methods such as Fast Low Angle SHot (FLASH) has been used for fast xenon imaging, however, none of these methods could provide a high resolution image.

In clinical regard, comparing to the other methods of perfusion measurement such as Arterial Spin Labeling (ASL) and Dynamic susceptibility contrast (DSC), xenon requires a considerable preparation. Polarized xenon cannot be stored for a long time (¡ 1-2 hours when frozen) so it should be either prepared minutes before the imaging which requires having access to a polarizer or transported from another source. Also, for the imaging purpose, a broadband imaging probe is required. Polarization takes 10-15 minutes which is a long time comparing to the short treatment window in stroke patients. Although polarized xenon has proven to be a powerful approach for lung and functional cardiac imaging, it might not be a convenient method for CBF measurement, especially in the presence of ASL and DSC imaging.

This project, therefore focused on finding a robust algorithm for the deconvolution process in DSC blood flow measurement. As we mentioned in the chapters I and III, the convolution model is an ill-posed integral equation which is very sensitive to noise. Many methods have been suggested improving this problem and to stabilize the solutions. These methods are referred to as regularization methods. Most of these methods work as low-pass filters and remove high frequency terms. Although this technique increases the stability, it causes underestimation in the solutions.

Currently, singular value decomposition based techniques are the most popular methods of deconvolution. Truncated SVD is one this methods, which is widely used for blood flow estimation and perfusion model deconvolution. It is very simple to implement and computationally inexpensive. However, there are two major challenges with this method. First, although it is clear that the truncation threshold, which defines the limits of the bandwidth of the filter, is proportional to the noise level, there is not yet a criterion for finding the optimum threshold. As we showed in the chapter III, the estimated flow rate is a sensitive function of this threshold value, and using a global value, introduces considerable error to the calculations. The protocol is to set the threshold it equal to 20% of the largest singular value. In most of the cases this threshold is too conservative and causes underestimation. The second issue with this method is that even at the optimum value of the threshold, solutions show some oscillations, which have no physical meaning. A more powerful regularization technique, Tikhonov regularization, is a 'small derivative' based regularization method that has the capability of generating smooth solutions. The fundamental assumption in this technique is that the solutions are smooth and their derivatives are small. Although residue functions are generally smooth functions, in low temporal or short mean transition time regimes this assumption is not valid. This gives rise to reduction in the slop of the decaying part of the residue functions which ultimately results in flow underestimation. We proposed the Generalized Tikhonov which can be used for any function, regardless of the nature of the function. In this approach we applied the filter to the difference of the solution and an expected residue function. This is an optimization method and the expectation residue function acts as the initial point for the optimization. The solutions can be used in iterative way to find the best result. In terms of divergence of the iterative method, it can be shown that it is equivalent

to the MLE (maximum likelihood estimation) and follows the same criteria in regard to the divergence issue. Also, we proposed another version of this method that the regularization receives its initial expectation residue function from a gamma-based function fitted to the results of a model-free method such as TSVD. One advantage of this method over the other two methods is the capability of the introducing priori information to the regularization. Although regular Tikhonov also take advantage of priori information on the smoothness of the residue functions, this model has the capability of going beyond the simple nature and includes other effects such as delay and dispersion. One criticism to this method, we expect to be on the issue of using a gamma-based function for the fit. The travel time between the two points through large number of discrete paths has been a famous problem communication, for example a phone call or a web surf between a user and a destination through different hubs, and is proved to be a gamma distribution. Bolus travel between the artery and a specific point in the tissue through the network of the capillaries is not a different problem. Also, this model is only used as an initial feed for the optimization and the only importance of the model here is to choose the initial values that are closer to the optimum value for faster, and when the is limit on the iterations, and more accurate results. Let's mention that Tikhonov uses several criteria for the regularization optimization. Quiet opposite to TSVD, Tikhonov has the capability of optimizing the regularization paramters locally, and pixel by pixel. This will prevent overfitting the solutions to the a priori information. Using simulations for different types of residue functions, it was showed that the method improves the regularization regardless of the type of the residue function. The second criticism could be the large amount of computation necessary for this method. There is a price to pay for a more sophisticated method. Currently, the processing takes almost 10-20 times

more than TSVD. This can be improved by tuning the code for faster calculations. Also, perfusion measurement is a very parallel problem. Separate pixels of the image can be treated independently from each other. With new multiprocessor computers we expect that the total time reduces to around one minute. Delay issue was also improved using two different approaches. The first approach which was adopted from Ibaraki et al. fitted the residue function to the gamma-based residue function and estimated the delay. Then the data is shifted and residue function was recalculated. This method showed promising, however, the initial residue function calculated for the fitting purpose was usually distorted and the fit was not very accurate. Also it is model based and in case of considerable deviation of the residue function from the model the estimated delay could be inaccurate. The second method, which we refer to that as limited elements shift matrix, calculates the delay with a blind optimization of a shift matrix that minimizes the residual term. The method combines interpolation and optimization. Technically the method can estimate the delay by optimizing minimum two elements, however, the accuracy increases when more elements are implemented. To investigate the accuracy of the mathematical method in actual experiments, we designed a microfabricated phantom that in terms of perfusion parameters is very similar to actual tissues. Experimental results showed the TSVD and the Generalized Tikhonov estimate flow rates more accurately than Tikhonov regularization. The major part of error in regular Tikhonov comes from the incapability of the L-curve criteria in finding the optimum value of the regularization parameter. In the presence of delay, again Tikhonov caused over-smoothed residue functions. Such over smoothings results in a considerable underestimation. TSVD dependence on the truncation threshold can dramatically affect the results. Lack of a criterion for finding a local truncation threshold is a serious problem in

this method and conservative values may result in even more than 40% reduction in the estimated flow rate.

In general, the phantom experiments showed that the perfusion related parameters are very sensitive to noise, delay, dispersion, temporal resolution and position of the sample. Although they accurately show the regions of reduced flow and mean transition time, they are not yet capable of precisely calculate the quantitative values. A small displacement of the sample can completely change the flow map, especially when the sample has a diverse density of capillaries and the image has a low resolution. This is even a challenege in *in vivo* perfusion imaging. A small error in the AIF measurement can give rise to large errors in estimated flows. Our experimental results implies that looking for indicators with more stability, and less sensitivity to their environment could be a possibility if it is proved that absolute blood flow values are essential for stroke treatments.

BIBLIOGRAPHY

BIBLIOGRAPHY

[1] J. A. P. A. Kuruc, S. Treves, C. Cheng, and A. Sawan. Radionuclide angiocardiography: an improved deconvolution technique for improvement after suboptimal bolus injection. *Radiology.*, 148(1):233–238, 1983.

[2] G. W. Albers. Expanding the window of thrombolytic therapy in acute stroke: The potential role of acute mri for patient selection. *Stroke*, 30:2230–2237, 1999.

[3] I. K. Andersen, A. Szymkowiak, L. G. H. C. E. Rasmussen, J. R. Marstrand, H. B. Larsson, and L. K. Hansen. Perfusion quantification using gaussian process deconvolution. *Magnetic Resonance in Medicine*, 48:351361, 2002.

[4] J. Astrup, B. K. Siesjd, and L. Symon. Thresholds in cerebral ischemia the ischemic. *Stroke A Journal of Cerebral Circulation*, 12(6):723–725, 1981.

[5] J. H. Bates. Deconvolution of tracer and dilution data using the weiner filter. *IEEE Transaction on Biomedical Engineering*, 38(12):1262–1266, 1991.

[6] J. Bock, P. Deuflhard, A. Hoeft, H. Korb, H.-G. Wolpers, J. Steinman, and G. Hellige. Thermal recovery after passage of the pulmonary circulation of the pulmonary circulation assessed by deconvolution. *J. Appl. Physiol.*, 64:1210–1216, 1988.

[7] R. Bogdanski, M. Blobner, H. Fink, and E. Kochs. Effects of xenon on mesenteric blood flow. *European Journal of Anaesthesiology*, 20(2):98–103, 2003.

[8] T. A. Bronikowski, C. A. Dawson, and J. H. Linehan. Model-free deconvolution techniques for estimating vascular transport functions. *Int J Biomed Comput.*, 14(5):411–429., 1983.

[9] K. Butcher, M. Parsons, T. Baird, A. Barber, G. Donnan, P. Desmond, B. Tress, and S. Davis. Perfusion thresholds in acute stroke thrombolysis. *Stroke*, 34:2159–2164, 2003.

[10] F. Calamante, D. G. Gadian, and A. Connelly. Quantification of bolus-tracking mri: Improved characterization of the tissue residue function using tikhonov regularization. *Magnetic Resonance in Medicine*, 50(6):1237–47, 2003.

[11] A. P. Dempster, N. M. Laird, and D. B. Rubin. Maximum likelihood from incomplete data via the em algorithm. *Journal of the Royal Statistical Society. Series B (Methodological)*, 39(1):1–38, 1977.

[12] B. L. Diffey, F. M. Hall, and J. R. Corfield. The 99mtc-dtpa dynamic renal scan with deconvolution analysis. *The Journal of Nuclear Medicine*, 17(5):352–355, 1976.

[13] B. Ebrahimi and T. E. Chupp. Compensated tikhonov regularization for quantitative perfusion measurements. *Proc. SPIE*, 6913:DOI:10.1117/12.770894, 2008.

[14] B. Ebrahimi, S. D. Swanson, and T. E. Chupp. The effect of noise and depolarization on hyperpolarized tracers perfusion assessment. *Proceedings of the 2007 IEEE International Symposium on Biomedical Imaging: From Nano to Macro, Washington, DC, USA, April 12-16*, pages 137–140, 2007.

[15] B. Ebrahimi, S. D. Swanson, B. Mosadegh, and T. E. Chupp. A perfusion phantom for quantitative medical imaging. *Proc. SPIE*, 6913:DOI:10.1117/12.770894, 2008.

[16] D. R. Emerson, K. Cieslicki, X. Gua, and R. W. Barber. Biomimetic design of microfluidic manifolds based on a generalised murrays law. *Lab on a Chip*, 6:447454, 2006.

[17] J. S. Fleming and B. A. Gorddard. A technique for the deconvolution of the renogram. *Phys Med Biol*, 19:546–549, 1974.

[18] G. Golub and W. Kahan. Calculating the singular values and pseudo-inverse of a matrix. *Journal of the Society for Industrial and Applied Mathematics: Series B, Numerical Analysis*, 2(2):205–224, 1965.

[19] F. Gorgins. Basic concepts in the determination of vascular volumes by indicator-dilution methods. *Circulation Research*, 10:429–446, 1962.

[20] C. B. Grandin, T. P. Duprez, A. M. Smith, F. Mataigne, A. Peeters, C. Oppenheim, and G. Cosnard. Usefulness of magnetic resonancederived quantitative measurements of cerebral blood flow and volume in prediction of infarct growth in hyperacute stroke. *Stroke*, 32:1147–1153, 2001.

[21] R. Gruner and T. Taxt. Iterative blind deconvolution in magnetic resonance brain perfusion imaging. *Magnetic Resonance in Medicine*, 55(4):805815, 2006.

[22] J. Hadamard. *Le problme de Cauchy et les quations aux drives partielles linaires hyperboliques*. Hermann, Paris, 1932.

[23] L. Hadley and J. R. Conn. Equilibrium distribution of radioxenon in tissue: xenon-hemoglobin association curve. *J Appl Physiol*, 16:1065–1070, 1961.

[24] P. C. Hansen. Analysis of discrete ill-posed problems by means of the l-curves. *SIAM*, 32(4):561–580, 1992.

[25] M. R. Hestenes. Inversion of matrices by biorthogonalization and related results. *Journal of the Society for Industrial and Applied Mathematics*, 6(1):51–90, 1958.

[26] E. G. Hoeffner. Cerebral perfusion imaging. *Journal of Neuro-Ophthalmol*, 25:313320, 2005.

[27] S. V. Huffel, J. Vandewalle, and J. M. W. M. Ch. De Roo. Reliable and efficient deconvolution technique based on total linear least squares for calculating the renal retention function. *Medical and Biological Engineering and Computing*, 25(1):26–33, 1987.

[28] E. Johansson, L. E. Olsson, S. Mansson, J. S. Petersson, K. Golman, F. Stahlberg, and R. Wirestam. Perfusion assessment with bolus differentiation: A technique applicable to hyperpolarized tracers. *Magnetic Resonance in Medicine*, 52(5):1043 – 1051, 2004.

[29] P. R. Johnston and R. M. Gulrajani. Selecting the corner in the -curve approach to tikhonov regularization. *IEEE Transaction on Biomedical Engineering*, 42:1293–1296, 2000.

[30] J. E. Juni, J. H. Thrall, J. W. Froelich, R. C. Wiggins, D. A. C. Jr, and M. Tuscan. The appended curve technique for deconvolutional analysismethod analysismethod. *Eur J Nucl Med*, 14:403–407, 1988.

[31] I. Kane, T. Carpenter, F. Chappell, C. Rivers, P. Armitage, P. Sandercock, and J. Wardlaw. Comparison of 10 different magnetic resonance perfusion imaging processing methods in acute ischemic stroke. *Stroke*, 38:3158–3164, 2007.

[32] G. S. Kassab and Y. Fung. Topology and dimensions of the pig coronary capillary network. *Am. J. Physiol. (Heart Circ. Physiol.)*, 36:H319–H325, 1994.

[33] S. Kety and C. Schmidt. The determination of cerebral blood flow in man by the use of nitrous oxide in low concentration. *Am. J. Physiol.*, 143:53–66, 1945.

[34] M. Koenig, M. Kraus, C. Theek, E. Klotz, W. Gehlen, and L. Heuser. Quantitative assessment of the ischemic brain by means of perfusion-related parameters derived from perfusion ct. *Stroke*, 32:431–437, 2001.

[35] E. Kogbetliantz. Diagonalization of general complex matrices as a new method for solution of linear equations. *Proc. Internat. Congress of Mathematicians*, 2:356–357, 1954.

[36] M. A. Konerding, E. Fait, and A. Gaumann. 3d microvascular architecture of pre-cancerous lesions and invasive carcinomas of the colon. *British Journal of Cancer*, 84(10):13541362, 2001.

[37] K. Kudo, S. Terae, C. Katoh, M. Oka, T. Shiga, N. Tamaki, and K. Miyasaka. Quantitative cerebral blood flow measurementwith dynamic perfusion ct using the vascular-pixel elimination method: Comparison with h2o(15). *AJNR Am J Neuroradiol*, 24:419–426, March 2003.

[38] N. N. Kuzma, B. Patton, K. Raman, and W. Happer. Fast nuclear spin relaxation in hyperpolarized solid 129xe. *Phys. Rev. Lett.*, 88(14):147602, 2002.

[39] M. Lu, Z. G. Zhang, and M. Chopp. Analysis of cerebral microvascular architectureapplication to cortical and subcortical vessels in rat brain. *Journal of Neuroscience Methods*, 138:8187, 2004.

[40] S. Mansson, E. Johansson, J. Svensson, L. E. Olsson, F. Stahlberg, and K. G. J. S. Petersson. Echo-planar mr imaging of dissolved hyperpolarized 129xe. *Acta Radiology*, 43(5):455–60, 2002.

[41] P. Meier and K. Zierler. On the theory of the indicator-dilution method for measurement of blood flow and textitvolume. *J. Appl. Physiol.*, 6(12):731–734, 1954.

[42] K. Mouridsen, K. Friston, N. Hjort, L. Gyldensted, L. Ostergaard, and S. Kiebelb. Bayesian estimation of cerebral perfusion using a physiological model of microvasculature. *NeuroImage*, 33:570–579, 2006.

[43] R. R. Moustafa and J. C. Baron. Pathophysiology of ischaemic stroke: insights from imaging, and implications for therapy and drug discovery. *British Journal of Pharmacology*, 153:S44–S54, 2008.

[44] D. G. Nabavi, L. M. LeBlanc, B. Baxter, D. H. Lee, A. J. Fox, S. P. Lownie, G. G. Ferguson, R. A. Craen, A. W. Gelb, and T. Y. Lee. Monitoring cerebral perfusion after subarachnoid hemorrhage using ct. *Neuroradiology*, 43:7–16, 2001.

[45] D. P. Oleary. Near optimal parameter for tikhonov and other regularization methods. *SIAM J. Sci. Comput.*, 23:411611171, 2001.

[46] L. Ostergaard, R. M. Weisskoff, D. A. Chesler, C. Gyldensted, and B. R. Rosen. High resolution measurement of cerebral blood flow using intravascular tracer bolus passages. part i: Mathematical approach and statistical analysis. *Magnetic Resonance in Medicine*, 36(5):715–725, 1996.

[47] G. Pawlik, A. Rackl, and R. J. Bing. Quantitative capillary topology topgraphy and blood flow in the cerebral cortex of cats: An in vivo microscopy study. *Brain Research*, 208:35–58, 1981.

[48] R. Puchalt, A. G. J. Pavia, and D. Ros. Optimal filtering values in renogram deconvolution. *Phys. Med. Biol.,*, 33(7):831–845, 1988.

[49] L. Rohl, L. Ostergaard, C. Z. Simonsen, P. Vestergaard-Poulsen, G. Andersen, M. Sakoh, D. L. Bihan, and C. Gyldensted. Viability thresholds of ischemic penumbra of hyperacute stroke defined by perfusion-weighted mri and apparent diffusion coefficient. *Stroke*, 32:1140–1146, 2001.

[50] G. Schlaug, A. Benfield, A. E. Baird, B. Siewert, K. O. Lovblad, R. A. Parker, R. R. Edelman, and S. Warach. The ischemic penumbra - operationally defined by diffusion and perfusion MRI. *Neurology*, 53:1528–1536, 1999.

[51] A. Umemura, T. Suzuka, and K. Yamada. Quantitative measurement of cerebral blood flow by 99mtc-hmpao spect in acute ischaemic stroke: usefulness in determining therapeutic options. *J Neurol Neurosurg Psychiatry*, 69(4):472478, October 2000 ;.

[52] M. E. Valentinuzzi and E. M. Volachec. Discrete deconvolution. *Medical and Biological Engineering and Computing*, 13(1):123–125, 1975.

[53] E. P. A. Vonken, F. J. Beekman, C. J. Bakker, and M. A. Viergever. Maximum likelihood estimation of cerebral blood flow in dynamic susceptibility contrast mri. *Magnetic Resonance in Medicine*, 41(2):343350, 1999.

[54] M. E. Wagshul and T. E. Chupp. Optical pumping of high-density rb with a broadband dye laser and gaalas diode laser arrays: Application to 3he polarization. *Physical review A*, 40(8):4447 – 4454, 1989.

[55] L. Willats, A. Connelly, and F. Calamante. Improved deconvolution of perfusion mri data in the presence of bolus delay and dispersion. *Magnetic Resonance in Medicine*, 56(1):146–156, 2006.

[56] M. Wintermark, M. Sesay, E. Barbier, K. Borbely, W. P. Dillon, J. D. Eastwood, T. C. Glenn, C. B. Grandin, S. Pedraza, J. Soustiel, T. Nariai, G. Zaharchuk, J. Caill, V. Dousset, and H. Yonas. Comparative overview of brain perfusion imaging techniques. *Stroke*, 36:2032–2033, 2005.

[57] R. Wirestam, L. Andersson, L. Ostergaard, M. Bolling, J. P. Aunola, A. Lindgren, B. Geijer, S. Holtas, and F. Stahlberg. Assessment of regional cerebral blood flow by dynamic susceptibility contrast mri using different deconvolution techniques. *Magnetic Resonance in Medicine*, 43(5):691 – 700, 2000.

[58] J. Wolber, I. J. Rowland, and A. B. M. O. Leach. Perfluorocarbon emulsions as intravenous delivery media for hyperpolarized xenon. *Magnetic Resonance in Medicine*, 41(3):442–449, 1999.

[59] O. Wu, L. Ostergaard, R. M. Weisskoff, T. Benner, B. R. Rosen, and A. G. Sorensen. Tracer arrival timing-insensitive technique for estimating flow in mr perfusion-weighted imaging using singular value decomposition with a block-circulant deconvolution matrix. *Magnetic Resonance in Medicine*, 50(1):164 – 174, 2003.